University of Twente

Master Thesis

Influence of tidal sand wave fields on wind wave propagation

ing. S.G. Overbeek

University of Twente

Master Thesis

Influence of tidal sand wave fields on wind wave propagation

ing. S.G. Overbeek

supervised by
ir. G.H.P. Campmans — dr. ir. P.C. Roos — prof. dr. ir. H.J. de Vriend — prof. dr. S.J.M.H. Hulscher

Study: Civil Engineering and Management
Department: Water Engineering and Management

July 14, 2016

image cover: Satellite image of the Southern Bight of the North Sea where sand wave fields occur. Image created by NASA.

Preface

This thesis is written as the final part of my study Water Engineering and Management at the University of Twente. After a four-year study of Civil Engineering at the University of Applied Science at Saxion in Enschede, followed by a one-year work experience at Waterschap Regge & Dinkel in Almelo, this study is, at least for now, the end of my educational career. During the past six months I worked on understanding the influence of sand wave fields on wind waves. This thesis is part of a more comprehensive work on the dynamics of sand waves which is of practical interest for safe ship navigation and optimizing dredging strategies. The theoretical and scientific approach of this thesis was an instructive period and hopefully I can apply the latter in practice in the near-future.

I want to acknowledge my gratitude to the people who helped me reach this point. First, I would like to thank Pieter Roos en Geert Campmans for their daily support, ideas and constructive feedback. Also, I would like to thank Suzanne Hulscher and Huib de Vriend for their ideas and guidance on this work. Furthermore I would like to thank my direct and indirect family and friends for their support and interest. In particular I would like to thank my girlfriend Sanne Kenter for her ideas and positivism during the road.

Sven Overbeek
Hengelo, July 2016

Abstract

Tidal sand waves are large-scale rhythmic bed forms commonly observed in tide-dominated shallow seas with a sandy seabed. Sand waves typically occur in fields as for example observed in the Southern Bight of the North Sea. They are here characterized by wavelengths between 100 and 1250 m, heights of 1 to 15 m and crests perpendicular to the principal direction of the tidal current. Due to morphological processes, sand waves grow and migrate which, in combination with the relatively small water depth of the North Sea, might result in interference with ship navigation, dredging activities and pipelines. Via near-bed orbital velocities, wind-generated surface gravity waves (i.e. wind waves) are able to interact with sand wave dynamics. The influence of a wavy bathymetry due to sand waves on the propagation of wind waves is not yet understood.

In this study the influence of sand wave fields on wind wave propagation is investigated. Therefore a model is described based on the elliptic partial differential equation called the Mild-Slope Equation by Berkhoff (1976). This theory assumes an irrotational and inviscid fluid, linear harmonic waves and no energy dissipation and describes shoaling and refraction effects. Also, the model assumes the absence of currents. Furthermore, the model is characterized by a square domain where monochromatic wind waves incident from one of the boundaries and where the other boundaries describe non-reflective boundary conditions based on the Sommerfeld Radiation Condition. In the middle of the domain a patch of sand waves is located surrounded by a flat-bed configuration such that the boundaries are located far away from the sand wave field. A finite difference approximation is used to discretize the model. The resulting system of linear equations is subsequently solved by a direct solution method. The model is verified with an analytical solution which exists in case of a flat-bed configuration.

The sand wave field is described by a bed elevation function that allows for variation in sand wave height, sand wave length, orientation with respect to the incident wind wave and asymmetry between the steep and mild slope. The patch-like structure is created by applying a 2D spatial tapering function.

The results show that the orientation of the sand wave crests with respect to the incident wind wave fronts has a major influence on the propagation of wind waves. Maximum influence is found when the sand wave crests are orientated perpendicular to the wind wave crests. The influence of the mean water depth, sand wave length, sand wave height and asymmetry becomes stronger when the orientation of the sand wave crests approaches perpendicularity. Furthermore, the influence of the mean water

depth, sand wave height and sand wave length is relatively strong whereas the influence of asymmetry is relatively small.

For regular patterns, amplifications up to three times the wind wave amplitude and three times the near-bed orbital flow velocity are found above perpendicular oriented sand wave crests with respect to the crest of the incident wind wave. Moreover, under certain parameter conditions local maxima were found indicating the presence of Bragg Resonance. In case of observed, irregular sand wave fields, wind waves also show amplification in amplitude and near-bed flow velocity. Furthermore, the zones of amplification of wind wave amplitude and near-bed orbital flow velocity are not always in union with the change of bed elevation.

Contents

List of Figures

List of Tables

List of Symbols

Overall

g	gravitational constant
h	variable water depth between still water level and the variable bed level
$\bar{h}$	undisturbed water depth between still water level and the flat bed level
i	imaginary unit (satisfying $i^2 = -1$)
L	length of the domain in x and y direction (equal length)
Ω_0	zone inside the domain with a flat bed
Ω_1	zone inside the domain with the sand wave field
t	time
x, y	horizontal coordinates
z	vertical coordinate

Sand waves

A_b	amplitude of the sand wave
α	angle of the stoss slope
β	angle of the lee slope
γ_0	parameter to determine the size of the flat bed zone
γ_t	parameter to determine the size of the transition zone between flat-bed and the sand wave field.
H_b	sand wave height
$\vec{k_b}$	topographic wave number vector
k_{bx}, k_{by}	counterparts of topographic wave number k_b in respectively x and y direction

k_{b1}, k_{b2} topographic wave numbers used for stoss and lee slope sinusoid

λ_b sand wavelength

$\lambda_{b1}, \lambda_{b2}$ horizontal length of respectively stoss and lee side ($\lambda_{b1} + \lambda_{b2} = \lambda = b$)

Ω_{1t} zone in the domain where tapering function $w_{2D}(x, y)$ (see below) should describe a linear gradient between 0 and 1

Ω_{1s} zone in the domain where tapering function $w_{2D}(x, y)$ (see below) should be 1

S_b asymmetry factor

φ_b phase of the sand wave

w_{2D} tapering function

z_b bed elevation

Wind waves

A_0 amplitude of the incident wind wave

$\mathrm{AF_A}$ amplification of wind wave amplitude

$\mathrm{AF_{nb}}$ amplification of near-bed orbital flow velocity

c phase celerity

c_g group celerity (envelope speed)

η surface elevation

$\hat{\eta}$ complex valued amplitude (phasor)

$\tilde{\eta}$ scaled complex valued amplitude

k wave number

K modified wave number

λ wavelength

ω angular frequency

Φ velocity potential beneath surface wave

$\hat{\Phi}$ complex velocity potential amplitude beneath surface wave

φ phase of the wind wave

T wave period

$\hat{u}_{\mathrm{nb}}$ complex near-bed orbital flow velocity in x direction

$\hat{v}_{\mathrm{nb}}$ complex near-bed orbital flow velocity in y direction

Chapter 1

Introduction

1.1 Tidal sand waves

Large parts of the bottom of a shallow shelf sea are covered with more or less regular bed forms (McCave, 1971; Terwindt, 1971). A classification of these bed forms, based upon spatial scale, is summarized in Table 1.1 where ripples are the smallest bed form, tidal sand banks the largest and tidal sand waves are found in between. Tidal sand waves are large-scale rhythmic bed forms which are commonly observed in tide-dominated shallow seas with a sandy seabed. Sand waves typically occur in fields which are for example observed in The Bahía Blanca Estuary in Argentina, the Adolphus Channel in Australia, the Strait of Messina in Italy, at the mouth of San Fransisco Bay in the U.S.A. and also in the Southern Bight of the North Sea (Figure 1.1) (Langhorne, 1973; McCave, 1971; Terwindt, 1971; Bijker et al., 1998; Aliotta and Perillo, 1986; Harris, 1989; Barnard et al., 2006; Santoro et al., 2002).

Due to the relatively small water depths of 17 to 55 meter at which sand wave fields are found in the Southern Bight of the North Sea, the wave height of sand waves, which is in the order of meters, can be significant. Furthermore, due to morphological processes, sand waves migrate and change in height and shape. The combination of these dynamics and the significant wave height makes the behaviour of sand waves of practical interest

Bed form	Wave length	Wave height	Migration speed	Time scale
Ripples	$0.1 - 1$ [m]	$0.01 - 0.1$ [m]	-	Hours
Beach cusps	$1 - 100$ [m]	$0.1 - 1$ [m]	-	Hours-days
Nearshore bars	$50 - 500$ [m]	$1 - 5$ [m]	$0 - 100$ [m/yr]	Days-weeks
Shoreface-connected sand ridges	$5 - 8$ [km]	$1 - 5$ [m]	$1 - 10$ [m/yr]	Centuries
Sand waves	**$300 - 700$ [m]**	**$1 - 5$ [m]**	**$1 - 10$ [m/yr]**	**Decades**
Tidal sand banks	$5 - 10$ [km]	$5 - 15$ [m]	-	Centuries
Long bed waves	1.5 [km]	5 [m]	Unknown	Unknown

Table 1.1: Rhythmic bed form characteristics in coastal seas (Dodd et al., 2003).

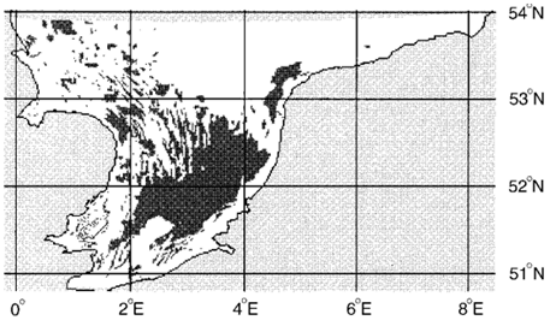

Figure 1.1: Location of sand wave fields (dark shading) in the Southern Bight of the North Sea (Hulscher and van den Brink, 2001).

for safe ship navigation, optimized dredging strategies and safe pipeline constructions.

Beside tidal currents, also wind-generated surface gravity waves (i.e. wind waves) can affect sand wave dynamics via near-bed orbital velocities. Conversely, due to the undulating bathymetry of sand wave fields and the shallow water depth, wind waves will feel the seabed and can therefore be affected by sand waves too. Hence, wind waves and sand wave fields interact in a two-way manner: top-down and bottom-up. In the present study, the bottom-up influence of a sand wave field on wind waves is investigated, as it is not yet understood.

In order to frame the content of this study, in this chapter, first the existing literature on this topic is briefly reviewed. Subsequently, the research objective and questions are introduced, together with the relevance of this study. Finally, the outline of the methodology together with a reading guide is addressed.

1.1.1 Characteristics

Sand waves fields have both one-dimensional and two-dimensional characteristics that can be used for quantification. A summary of these characteristics is given below.

Sand wave height is the vertical distance between the crest and trough of a sand wave and is throughout this thesis denoted with the symbol H_b. Within a sand wave field spatial variability of wave heights can be found. Sand wave heights in the North Sea range between 1 and 15 meter (McCave, 1971; Terwindt, 1971; Bijker et al., 1998; Németh et al., 2002; Dodd et al., 2003; Dijk and Kleinhans, 2005; Santen et al., 2011).

Sand wave length is the horizontal length between between two sand wave crests (or troughs) and is in this thesis denoted with the symbol λ_b. Also a variety of wavelengths are possible within a sand wave field. Literature on sand waves in the North Sea described sand wave lengths ranging between 100 and 1250 meter (McCave, 1971; Terwindt, 1971; Bijker et al., 1998; Németh et al., 2002; Dodd et al., 2003; Dijk and Kleinhans, 2005; Santen et al., 2011).

Migration of sand waves is caused by morphodynamic processes, i.e. the dynamics between topography and hydrodynamics. Literature on sand waves in the North Sea gave an indication of migration between 0 and 25 meter per year (McCave, 1971; Bijker et al., 1998; Németh et al., 2002; Dodd et al., 2003; Dijk and Kleinhans, 2005; Besio et al., 2008; Santen et al., 2011). Hence migration of sand waves is slow such that the time-scale of displacement of a whole bed form cycle is in the order of decades. A brief explanation on morphodynamic processes of sand waves is given in section 1.1.2. In this thesis, sand waves are assumed to be static.

Asymmetry between the steep and mild slope of the sand wave is throughout this thesis denoted with the symbol S_b, which is the ratio of the stoss and lee slope of the sand wave. Stoss is here defined as the slope of the sand wave which faces the incident wind wave. Sand waves are often simplified for mathematical purposes to a sinusoid with a perfect symmetric shape. In reality sand waves often have an asymmetric profile with a steep- and a mild slope (Terwindt, 1971). According to Besio et al. (2004), this asymmetry is caused by the presence of a residual current caused by for example asymmetry of the tidal wave. Furthermore, an asymmetric sand wave profile is an indicator for migration (Besio et al., 2008). Knaapen (2005) used asymmetry as a predictor for sand wave migration and summarized the degree of asymmetry for different locations in the Southern Bight of the North Sea. Although another assymetry factor was used[1], the observations in Knaapen (2005) correspond to values of S_b between 1 and 3, which means that the longest side of the sand waves can be upto three times as long as the short side.

Roughness caused by the surface structure is another characteristic of a sand wave as it is relevant in hydrodynamic calculations. Dijk and Kleinhans (2005) analysed the grain sizes found in sand waves and found grain sizes ranging between 178 and 510 micrometer[2]. Furthermore, often superimposed megaripples with heights upto the height of sand waves itself are found on sand waves which cause a deformed shape and more roughness (Catano-Lopera and Garcia, 2006). In this thesis roughness is not taken into account.

Orientation of the sand wave crests is another important characteristic and is throughout this thesis denoted with the symbol θ_b. Within a sand wave field, the crests are almost (slightly deviated anti-clockwise) orientated perpendicular to the tidal current (Hulscher et al., 1993). Németh et al. (2006) quantified this orientation to deviate up to 10 degrees anti-clockwise from the direction of the principle current. Furthermore the orientation of the crests can vary in a sand wave field due to changing sub-tidal conditions for example induced by tidal sand banks (Hulscher and van den Brink, 2001).

[1] Knaapen (2005) used the asymmetry factor $A_s = \frac{\lambda_{b2}-\lambda_{b1}}{\lambda_{b1}+\lambda_{b2}}$. For nomenclature see Figure 3.1.

[2] lowest value is the D_{10} average grain diameter found at a coastal site, highest value is the D_{90} average grain diameter found at an offshore site.

Spatial variability of a sand wave field is the last characteristic. Variability by for example varying orientations, wave heights and wavelengths will cause irregular sand wave field patterns. Also, bifurcations, which are points where a sand wave crests splits into two sand wave crests, are commonly present (Langhorne, 1973). Dorst et al. (2011) statistically assessed the spatial variability by a deformation analysis, and concluded that sand wave behaviour is strongly variable over a continental shelf with correlations that are not yet understood.

1.1.2 Morphodynamics

Sand waves grow and migrate due to morphodynamic processes. The predominant hydrodynamic influence is exerted by tidal currents which produce an oscillating movement in the horizontal plane. This reciprocating flow is uniform in case of a (unrealistic) flat-bed configuration, but in case of a perturbation on the flat-bed, uniform conditions are absent and therefore vertical flow will be present. Hulscher (1996) studied the growth of small perturbations resembling sand waves and sand banks by means of a linear stability analysis. It was herein found that the perturbed near-bed flow stimulates growth as they produce, tide-averaged, a trough-to-crest movement. Because of this trough-to-crest movement, sediment particles tend to drag towards the crest of the sand wave whereas gravity tends to pull the sediment back down to the trough. Furthermore, when a residual current or higher harmonic (e.g. M4 tidal constituent) is present, the sand waves can develop an asymmetric shape and can migrate in the direction of the residual current (Besio et al., 2004). Also, wind generated surface gravity waves can cause a residual current (Stokes drift) and therefore are able to cause migration of sand waves.

1.1.3 Influence of sand wave patterns on wind waves

When two fluid layers, moving at different speeds, are in contact with each other, a shear stress will be present and cause transfer of momentum and energy. Whenever wind blows over water, this might give rise to the formation of wind-generated surface gravity waves. In this study the focus lays on wind-generated surface gravity waves and are for the sake of brevity hereafter called *wind waves*.

A distinction can be made in terms of direct and indirect wind waves. Direct wind waves are generated by local winds. Indirect waves are also known as swell and are remains of waves generated elsewhere which have travelled a far distance from their origin, typically characterized by wavelengths between 300 and 600 meter and wave heights of centimeters (The Open University, 1999). Swell is not assessed in this study.

A data analysis of hourly wave data (period 1989 to 2010) from two measuring platforms[3] in the Southern Bight of the North Sea, gave insight in wave periods and significant wave height of wind waves[4] (Rijkswaterstaat, 2015). It showed average wave periods of 3 to 5 seconds and maximum wave periods of 10 to 11 seconds. Furthermore

[3] K13 alpha platform ($53°13.05'N 3°13.12'E$) and EURO platform ($51°59.88'N 3°16.49'E$).

[4] The significant wave height is the mean wave height of the highest one-third of the wave spectrum per time interval.

an average signficant wave height of 1 to 2 meter was found with a maximum of 7 to 8 meter.

When a wind wave propagates over an sand wave field, several processes are influencing the behaviour of the wind wave. The water column underneath wind waves experience orbital motion, that decreases with water depth. In case of shallow to intermediate water depth, the propagation of the wind wave is affected because this orbital motion is influenced by the seabed. Due to the undulating bathymetry of sand wave fields, the propagation speed (i.e. celerity or phase speed) of wind waves is locally changing when passing the sand wave field and therefore deformation of the shape of the wind waves is possible. The celerity of a wind wave can be expressed as follows:

$$c = \frac{\lambda}{T} = \frac{\omega}{k}, \tag{1.1}$$

where λ is the wind wave length, T is the wind wave period, $\omega = 2\pi/T$ is the angular frequency and $k = 2\pi/\lambda$ is the wind wave number.

In case of a uniform water depth, wind waves are not deformed and therefore have a permanent form and small amplitude. Under the assumption of a uniform depth and small ratio of wave height to water depth, George Biddell Airy published a theory nowadays known as *Airy theory* or *Linear Wave Theory*. Furthermore the theory assumes an irrotational, incompressible and inviscid fluid.

According to Linear Wave Theory the angular frequency and wave number are related to each other by the dispersion relationship:

$$\omega^2 = gk \tanh(kh), \tag{1.2}$$

where g is the gravitational acceleration and h is the variable water depth. Furthermore, inside a wave train different celerities might be present and therefore the envelope of the wave train becomes distorted. The speed at which this envelope travels is called the group celerity and can be expressed as follows:

$$c_g = \frac{d\omega}{dk}. \tag{1.3}$$

Using Eq. (1.2) and (1.3) the group celerity can then be expressed as:

$$c_g = \frac{\omega}{2k}\left(1 + kh\frac{1 - \tanh^2(kh)}{\tanh(kh)}\right). \tag{1.4}$$

This group celerity is also the velocity at which wave energy travels (Longuet-Higgins and Stewart, 1964). Therefore it is, in combination with conservation laws, used to formulate wave behaviour.

The aforementioned fundamental properties of wind waves cause that the following processes can occur whenever a wind wave propagates over a sand wave field:

Shoaling is the change of wind wave height due to an increase of energy density of the wind wave. The group celerity of the wave train decreases which, due to

conservation of energy flux, results in a higher energy density of the wind waves and hence an increase of wind wave height. Shoaling concerns large length scales (i.e. wave train deformation instead of individual wave deformation).

Refraction is another process related to the conservation of energy flux. The process of refraction tends to bend a wave crest to an alignment parallel with depth contours (The Open University, 1999). When water depth varies beneath a single wave crest, the wind wave propagates with varying celerties and hence the part of the crest in deep water travels faster than the part in shallow water and therefore the crest rotates.

Diffraction is the phenomena that happens when a wind wave encounters an obstacle, bends around it, and propagates into the shadow-zone of the obstacle.

Reflection of waves happens when the waves encounter an obstacle. When wind waves are incident on an wavy bathymetry such as sand wave fields, energy may be backscattered by the bed forms (Davies and Heathershaw, 1983). Under certain conditions, when the backscattered wave component is in phase with another wave component, both signals might show constructive interference (i.e. superposition). The latter is called **Bragg Resonance** and occurs when the wind wave length is twice the sand wave length (Davies and Heathershaw, 1983; Liu and Yue, 1998).

Wave-current interaction between for example tidal currents and wind waves will cause that energy is exchanged and will therefore influence wind waves by a Doppler shift (Peregrine, 1976). The interaction of wind waves and currents can be coupled by using a radiation stress tensor which requires depth- and phase averaging of the wind waves (Longuet-Higgins and Stewart, 1964).

Wave breaking causes wave energy dissipation and occurs when the wind wave height is greater than a certain proportion of the water depth and is therefore depth-induced. **White-capping** also dissipates wave energy and is the breaking of the top induced by the steepness of the wind wave.

Bottom friction will influence the behaviour of the wind wave when the water depth is shallow such that wind waves feel the seabed. Due to form drag (i.e. friction due to bed forms such as megaripples) and skin friction (i.e. friction due to grain roughness) caused by the seabed the orbital motion is suppressed. However, friction forces are generally small for short waves (i.e. wind waves) and are therefore often neglected (Dingemans, 1994; Dalrymple et al., 1989).

Viscosity of the fluid causes that energy dissipates. Generally, viscous effects are only normative in the thin bottom boundary layer. For the main body of the fluid viscous effects can be neglected and therefore an inviscid fluid and subsequently an irrotational fluid can be assumed (Dean and Dalrymple, 1991).

In order to assess the simultaneous effect of several of the aforementioned processes, Berkhoff (1976) derived a partial differential equation called the *Mild-Slope Equation*

that is able to calculate the combined effect of shoaling, refraction, diffraction and reflection for (wind) waves over an uneven bathymetry. This theory is only valid in case of irrotational, linear harmonic waves and does not consider energy dissipation due to friction or wave breaking (Berkhoff, 1972). Moreover, the Mild-Slope Equation assumes that the vertical structure of the surface wave slowly changes in the horizontal plane such that horizontal derivatives can be neglected in the formulation of the bottom boundary condition (Berkhoff, 1976). Dingemans (1994) quantified this restriction as:

$$\frac{|\nabla h(x,y)|}{kh} \ll 1. \tag{1.5}$$

Hence, as the name already reveals, a mildly sloping bathymetry is required. Booij (1983) verified the mild-slope equation with a fully three-dimensional equation and concluded that the mild-slope equation still produces good results for bottom inclinations upto 1:3, which however seems rather steep.

Literature provides the Mild-Slope Equation in elliptic (i.e. time-independent), hyperbolic (i.e. time-dependent) and parabolic forms (Berkhoff, 1976; Dingemans, 1994; Radder, 1979). The parabolic formulation reduces computational cost but is limited to wind waves propagating nearly along a given direction and thus will obliquely incident wind waves result in significant errors (Dalrymple et al., 1989). Furthermore, the literature provides many more extended or modified forms of the Mild-Slope Equation that account for example for energy dissipation or non-linear effects. In this study, the elliptic Mild-Slope Equation is used to formulate the behaviour of wind waves over sand wave fields.

Besides the Mild-Slope Equation, also Boussinesq type model equations can be used to mathematically describe wind wave motion over an undulating bathymetry. The Boussinesq equations are valid for weakly non-linear waves, a shallow to intermediate water depth and fairly long wave lengths (Dingemans, 1994; Sharifahmadian, 2015). Furthermore, the dispersion relation used in the Boussinesq equations are somewhat crude, however improved versions are derived in literature (Dingemans, 1994). The Mild-Slope Equation and Boussinesq type equations describe wave motion in the horizontal plane with depth-integration, however when the variations in depth are important the full three-dimensonal Navier-Stokes equations should be used (Sharifahmadian, 2015). The Navier-Stokes equations are rather complicated and require much computational cost to solve. Furthermore, Due to the freedom of choice in water depth and wavelength, the Mild-Slope Equation is chosen over the more cumbersome Boussinesq equations.

1.2 Research objective and questions

The research objective of this study reads:

To investigate the influence of sand wave fields in a shallow sea on incident monochromatic wind waves.

To reach this objective the following research question is formulated:

1. What is the influence of sand wave fields on monochromatic wind waves and how can this influence be visualized and quantified?
   (a) What is the spatial variability of surface elevation and near-bed orbital velocities above a sand wave field and how can this be visualized and quantified?
   (b) What parameters are dominating the spatial variability in surface elevation and near-bed orbital velocities?
   (c) Which configurations of input parameters show a significant influence?

1.3 Relevance

Sand waves are dynamic and therefore accurate knowledge about these dynamics is necessary to ensure safe ship navigation, optimize dredging strategies and safe pipeline constructions. Via near-bed orbital velocities, wind waves are able to interact with sand wave dynamics and therefore this interaction is of practical interest to model sand wave dynamics.

In order to improve the navigation safety in the North Sea, the SMARTSEA-project has been set-up which is funded within the TKI Maritime Call of NWO-STW (STW, 2014). One of the aims in this multidisciplinary project is to better understand the influence of storm events and wind waves on sand wave dynamics. In order to fully understand the influence of wind waves on sand wave dynamics, it is also necessary to investigate the bottom-up influence of sand waves on wind waves because wind waves and sand wave interact in a two-way manner.

This study is relevant as it will investigate whether the presence of a physically bounded sand wave field will influence the propagation of the wind waves. This will lead to insights in spatial variability of the wind waves induced by the variable bathymetry. The process of shoaling, refraction and reflection can locally increase or decrease the wind wave height such that subsequently the top-down influence via near-bed velocities of wind waves on sand waves can locally strengthen or weaken.

Furthermore, this study will give insight about what characteristics of a sand wave field dominantly influence wind waves and what patterns are visible at the water surface. Subsequently, this knowledge can be used to find out under which circumstances the change of wind wave conditions induced by the sand wave field, becomes normative in the dynamics of sand waves. Also, possibly the outcomes of this study can be used to extent the knowledge on mapping bathymetric data via changing water surface conditions.

1.4 Outline of methodology and reading guide

In order to answer the research question, first, a hydrodynamic model is set-up such that the influence of sand wave fields on the propagation of wind waves can be assessed. Under the assumption of an irrotational, inviscid and incompressible water body and the absence of currents and dissipative terms as bottom friction and wave breaking, the elliptic Mild-Slope Equation is used to formulate the hydrodynamic model in Chapter

2. Subsequently, the model domain and boundary conditions are formulated. Then, the numerical formulation of the hydrodynamic model is discussed. The latter is done by discretizing the governing model equation using finite differences and subsequently solving the linear system of equations with a direct solution method. Lastly, the hydrodynamic model is verified using an analytical solution in a highly simplified case.

Secondly, a bathymetric data set representing the sand wave field, is used as input for the hydrodynamic model. Due to the relatively slow migration and growth rate of sand waves compared to the propagation speed of wind waves the bathymetry is assumed to be static. In order to generate a regular sand wave field pattern, a bed elevation function is formulated in Chapter 3 that allows for variation in sand wave orientation with respect to the incident wind wave, sand wave length, sand wave height and sand wave asymmetry. Also, A tapering function will be used to generate the patch-like sand wave field surrounded by a flat-bed configuration towards the edges of the domain to minimize undesired interference at the boundary.

In Chapter 4, the influence of sand wave fields on monochromatic wind waves will be analysed by assessing different sand wave field configurations and incident wind waves. A visualization of the spatial variability will be given which is subsequently quantified. The influence of the parameters is summarized and compared in a sensitivity analysis. Also, possible situations of Bragg Resonance and the influence of natural (irregular) sand wave fields are assessed.

In Chapter 5 the Discussion is presented. Finally in Chapter 6 the conclusions and recommendations are given.

Chapter 2

Model formulation

In this chapter the hydrodynamic model, used to assess the influence of sand wave fields on wind waves, is described. In case of a mildly sloping seabed, the behaviour of wind waves can be modelled by means of a partial differential equation called the *Mild-Slope Equation*, derived by Berkhoff (1976). In Section 2.1, this Mild-Slope Equation is treated as it is the governing model equation. Subsequently, the model set-up is introduced which includes the formulation of the required boundary conditions. Then, in Section 2.3 the numerical formulation of the model is described. Therefore in Subsection 2.3 finite difference is used to discretize the model equations. Subsequently in Subsection 2.4 the direct solution method is explained used to solve the system of equations. Finally in Subsection 2.5 the model is verified with the use of an analytical solution.

2.1 Governing model equation

Under the assumption of linear harmonic waves, the classical, elliptic form of the Mild-Slope Equation describes the combined effect of refraction and diffraction over a mildly sloping bathymetry (see Eq. (1.5)). It is only valid in case of an irrotational fluid and does not consider energy dissipation due to friction or wave breaking. The elliptic Mild-Slope equation solves the time-independent, complex valued amplitude $\hat{\eta}(x, y)$ of which the surface elevation $\eta(x, y, t)$ (time-dependent) can be derived according to:

$$\eta(x, y, t) = \Re\{\hat{\eta} e^{-i\omega t}\}, \tag{2.1}$$

where $\Re$ denotes the Real part, i is the imaginary unit, ω is the angular frequency and t is time. The complex valued amplitude describes essentially the time-independent part of a complex wave signal, also known as the phasor. A more extensive explanation of the complex valued amplitude can be found in Appendix A.1.

The elliptic Mild-Slope Equation, according to Berkhoff (1976), reads:

$$\nabla \cdot (cc_g \nabla \hat{\eta}) + k^2 cc_g \hat{\eta} = 0, \tag{2.2}$$

where $\nabla = (\frac{\partial}{\partial x}, \frac{\partial}{\partial y})$ applied to a two dimensional scalar field represents the horizontal gradient, $\nabla\cdot$ the divergence operator, $c(x, y)$ the phase celerity, $c_g(x, y)$ the group celerity

and $k(x, y)$ the wave number. The dispersion relationship in Eq. (1.2) according to *Linear Wave Theory* is used to express the relation between the wave number and angular frequency. With Eq. (1.1) and (1.4), which are based on this dispersion relationship, the product cc_g can be formulated as:

$$cc_g = \frac{1}{2}\left(\frac{\omega}{k}\right)^2 \left(1 + kh\frac{1 - \tanh^2(kh)}{\tanh(kh)}\right), \tag{2.3}$$

where $h(x, y)$ is the variable water depth and is dependent on the bed elevation caused by the sand wave field. The function determining $h(x, y)$ is introduced in Chapter 3. The elliptic Mild-Slope equation in Eq. (2.2) can be reduced to a Helmholtz-equation without loss of generality. Radder (1979) introduced the required transformations to obtain the so-called *reduced Mild-Slope Equation*. This form reads:

$$\nabla^2\tilde{\eta} + K^2\tilde{\eta} = 0, \tag{2.4}$$

where ∇^2 is the Laplace operator. The following transformations were used:

$$\tilde{\eta} = \hat{\eta}\sqrt{cc_g}, \qquad K^2(x, y) = k^2 - \frac{\nabla^2\sqrt{cc_g}}{\sqrt{cc_g}}. \tag{2.5}$$

In these formulations, $\tilde{\eta}$ is the modified complex amplitude and K is a modified wave number which can be calculated beforehand and depends, through the water depth $h(x, y)$, on the horizontal coordinates x and y. The formula as presented in Eq. (2.4) will be used for the mathematical problem statement in Section 2.2.

Furthermore, due to the assumption of an irrotational fluid, a velocity potential Φ can be used to describe the vertical flow-structure beneath the wind wave, which is according to Linear Wave Theory:

$$\Phi(x, y, z, t) = \Re\{\hat{\Phi}(x, y, z)e^{-i\omega t}\}, \qquad \hat{\Phi}(x, y, z) = \frac{g}{i\omega}\frac{\cosh(k[h + z])}{\cosh(kh)}\hat{\eta}(x, y), \tag{2.6}$$

where $\hat{\Phi}$ is the complex valued velocity potential, z is the vertical coordinate and g is the gravitational acceleration. Subsequently when taking the horizontal derivative of this velocity potential one can obtain the orbital velocity beneath the wave. Finally, because of the elliptic form of the Mild-Slope equation, boundary conditions are required at all boundaries enclosing the model domain. The behaviour of the Mild-Slope equation is controlled by proper formulation of the complex valued amplitude on these boundaries, hence making it a *Boundary Value Problem*. The boundary conditions are formulated in Section 2.2.

2.2 Model domain and boundary conditions

In order to assess the influence of sandwave fields on wind waves, a model is formulated. This model has a square domain of length L in both directions and consists of two

zones. The zone Ω_0 with a flat-bed configuration and the zone Ω_1 with the sand wave field patch. A sketch of the model domain is given in Figure 2.1. The zone with the flat-bed configuration is established to minimize the influence of the sand wave field near the boundaries (i.e. constant $h(x, y)$) such that physically realistic boundary conditions can be imposed more easily. Furthermore, the wind waves are chosen to enter the domain through the West boundary Γ_{west} and with its crests always perpendicular to the y coordinate. An arbitrary orientation of the wind wave crests with respect to the sand wave field will be captured in the orientation of the sand wave field itself (see Chapter 3). However, when the sand wave field is rotated inside Ω_1 this will also change the appearance of the sand wave field (e.g. for instance more crest length is present).

Inside the model domain, the reduced Mild-Slope equation given by Eq. (2.4) is governing which requires formulation of the transformed complex wave amplitude $\tilde{\eta}$ on the boundaries. At the West boundary condition we prescribe the transformed complex valued amplitude of the incident wind wave, which when assuming crests parallel to the y coordinate and a phase such that that crest is at the domain edge, results in the following *Dirichlet* type boundary condition on the West:

$$\tilde{\eta} = \tilde{A}_0, \qquad \tilde{A}_0 = A_0\sqrt{cc_g}, \qquad \text{at } \Gamma_{\text{west}}, \tag{2.7}$$

where $\tilde{A}_0$ is the transformed amplitude of the incident wind wave and A_0 is the (non-scaled) amplitude of the incident wind wave. The other boundaries need to represent

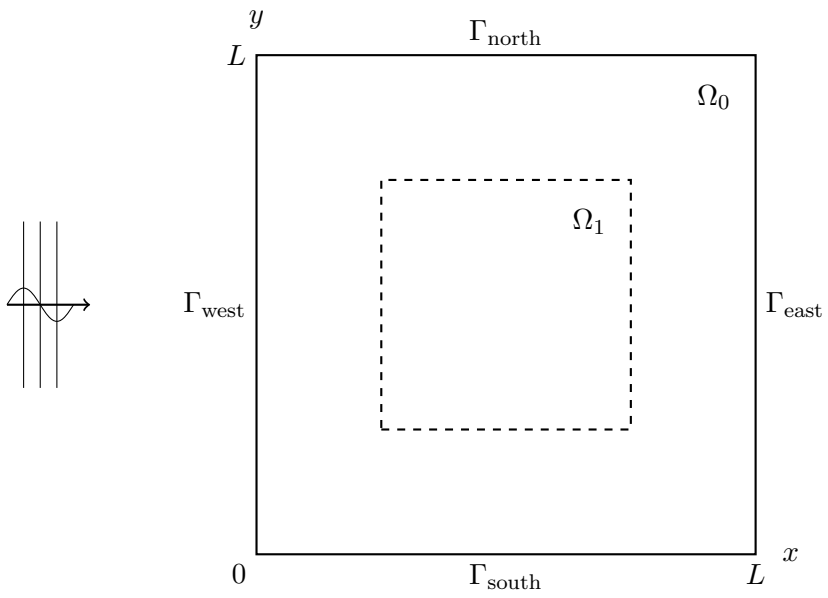

Figure 2.1: Sketch of the model set-up. Ω_1 represents the zone where the sand wave field is located including the tapering (see Section 3.4, hence cc_g is variable here. Ω_0 represents a zone with a flat bed configuration, hence cc_g is constant here. Furthermore, Γ represents a boundary.

open sea and should actually describe behaviour of the wind wave propagating progressively. Therefore *Non-reflective boundary conditions* (also reffered as *Artificial Boundary Conditions* or *Open Boundary Conditions*) need to be imposed on the North (Γ_{north}), East (Γ_{east}) and South (Γ_{south}) boundaries. An often used non-reflective boundary condition is derived from the Sommerfeld Radation Condition, named after *Arnold Sommerfeld*, which states that when waves at a source radiate to infinity, no energy should be reflected. For a Cartesian coordinate system and a boundary at a finite distance, this Sommerfeld radiation condition in terms of complex amplitudes is expressed as:

$$\frac{d\tilde{\eta}}{dn} = iK\cos(\theta_i)\tilde{\eta}, \tag{2.8}$$

where n is the inward normal with respect to the boundary and θ_i is the angle of the incident wind wave with respect to this normal (Tsay and Liu, 1983; Givoli, 1991; Oliveira, 2004; Panchang and Pearce, 1991). For the South and North boundaries these angles are respectively -90 and 90 degrees, such that Eq. (2.8) reduces to a *Neumann* type boundary condition:

$$\frac{d\tilde{\eta}}{dy} = 0 \qquad \text{at } \Gamma_{\text{south}}, \tag{2.9}$$

$$\frac{d\tilde{\eta}}{dy} = 0 \qquad \text{at } \Gamma_{\text{north}}. \tag{2.10}$$

At the East boundary condition, the angle is 0 degrees and therefore Eq. (2.8) describes a boundary condition of *Robin* type:

$$\frac{d\tilde{\eta}}{dx} = iK\tilde{\eta} \qquad \text{at } \Gamma_{\text{east}}. \tag{2.11}$$

2.3 Discretization using finite differences

For the numerical formulation of the model equations we choose for the finite difference method. An equidistant grid is chosen such that $\Delta = \Delta x = \Delta y$. The discretizations of the derivatives at a grid node are approximated using a *Taylor Series*. Four different kind of finite difference approximations, all being fourth order accurate, are used. The latter essentially means that four degrees of freedom are used to formulate a derivative of a local grid node assuming a certain accuracy. Unfortunately, attempts to discretize the derivatives by lower order accurate discetizations, which require less computational cost, led to unacceptable errors when keeping the number of grid nodes equal as will be shown in Section 2.5.

The square grid of size $\Omega_0 = [L, L]$, is numbered by by $m = [1, N]$ and $n = [1, N]$ elements in respectively x and y direction. Hence, (x_1, y_1) denotes the South-Western most grid node and (x_N, y_N) denotes the North-Eastern most grid node.

Discretization of derivatives

Below the used discretizations are given to determine the derivatives evaluated at base point (x_m, y_n). The discretizations of the second order derivatives over respectively x and y by a central spaced finite difference discretization, fourth order accurate are given below and is visualized in Figure 2.2a.

$$\left.\frac{d^2\tilde{\eta}}{dx^2}\right|_{x_m,y_n} = \frac{-\frac{1}{12}\tilde{\eta}_{x_{m-2},y_n} + \frac{4}{3}\tilde{\eta}_{x_{m-1},y_n} - \frac{5}{2}\tilde{\eta}_{x_m,y_n} + \frac{4}{3}\tilde{\eta}_{x_{m+1},y_n} - \frac{1}{12}\tilde{\eta}_{x_{m+2},y_n}}{\Delta^2} + \mathcal{O}(\Delta^4), \tag{2.12}$$

$$\left.\frac{d^2\tilde{\eta}}{dy^2}\right|_{x_m,y_n} = \frac{-\frac{1}{12}\tilde{\eta}_{x_m,y_{n-2}} + \frac{4}{3}\tilde{\eta}_{x_m,y_{n-1}} - \frac{5}{2}\tilde{\eta}_{x_m,y_n} + \frac{4}{3}\tilde{\eta}_{x_m,y_{n+1}} - \frac{1}{12}\tilde{\eta}_{x_m,y_{n+2}}}{\Delta^2} + \mathcal{O}(\Delta^4). \tag{2.13}$$

The discretizations of the second order derivatives over respectively x and y by an off-centered finite difference discretization, fourth order accurate are required for the near-boundary grid nodes and are given below and visualized in Figure 2.2b.

$$\left.\frac{d^2\tilde{\eta}}{dx^2}\right|_{x_m,y_n} = \frac{1}{\Delta^2}\left(\frac{10}{12}\tilde{\eta}_{x_{m-1},y_n} - \frac{15}{12}\tilde{\eta}_{x_m,y_n} - \frac{4}{12}\tilde{\eta}_{x_{m+1},y_n} + \frac{14}{12}\tilde{\eta}_{x_{m+2},y_n} - \frac{6}{12}\tilde{\eta}_{x_{m+3},y_n} + \frac{1}{12}\tilde{\eta}_{x_{m+4},y_n}\right) + \mathcal{O}(\Delta^4), \tag{2.14}$$

$$\left.\frac{d^2\tilde{\eta}}{dy^2}\right|_{x_m,y_n} = \frac{1}{\Delta^2}\left(\frac{10}{12}\tilde{\eta}_{x_m,y_{n-1}} - \frac{15}{12}\tilde{\eta}_{x_m,y_n} - \frac{4}{12}\tilde{\eta}_{x_m,y_{n+1}} + \frac{14}{12}\tilde{\eta}_{x_m,y_{n+2}} - \frac{6}{12}\tilde{\eta}_{x_m,y_{n+3}} + \frac{1}{12}\tilde{\eta}_{x_m,y_{n+4}}\right) + \mathcal{O}(\Delta^4). \tag{2.15}$$

Note that the discretizations in Eq. (2.14) and (2.15) are here denoted for the West and South near-boundary respectively. The same coefficients apply when flipping the indices to obtain respectively the discretization for the East and North near-boundary condition.

Finally, discretizations for the first order derivatives over respectively x and y, fourth order accurate, required for the formulation of the boundaries, are given below and visualized in Figure 2.2c.

$$\left.\frac{d\tilde{\eta}}{dx}\right|_{x_m,y_n} = \frac{\frac{25}{12}\tilde{\eta}_{x_m,y_n} - 4\tilde{\eta}_{x_{m-1},y_n} + 3\tilde{\eta}_{x_{m-2},y_n} - \frac{4}{3}\tilde{\eta}_{x_{m-3},y_n} + \frac{1}{4}\tilde{\eta}_{x_{m-4},y_n}}{\Delta} + \mathcal{O}(\Delta^4), \tag{2.16}$$

$$\left.\frac{d\tilde{\eta}}{dy}\right|_{x_m,y_n} = \frac{\frac{25}{12}\tilde{\eta}_{x_m,y_n} - 4\tilde{\eta}_{x_m,y_{n-1}} + 3\tilde{\eta}_{x_m,y_{n-2}} - \frac{4}{3}\tilde{\eta}_{x_m,y_{n-3}} + \frac{1}{4}\tilde{\eta}_{x_m,y_{n-4}}}{\Delta} + \mathcal{O}(\Delta^4). \tag{2.17}$$

Note that the discretizations in Eq. (2.16) and (2.17) are one-sided (backward) finite difference and applicable to the East and North boundary condition respectively. However, when giving the coefficients the opposite sign and flipping the indices, the forward finite difference discretizations which can be used for the formulation of the West and South boundary condition is obtained.

Stencils

Substituting the discretization of the derivatives in Eq. (2.4), the numerical formulation as given below results. The corresponding stencil is depicted in Figure 2.2a.

$$-\frac{1}{12}\tilde{\eta}_{x_m,y_{n-2}}-\frac{1}{12}\tilde{\eta}_{x_{m-2},y_n}+\frac{4}{3}\tilde{\eta}_{x_m,y_{n-1}}+\frac{4}{3}\tilde{\eta}_{x_{m-1},y_n}+(K^2_{x_m,y_n}\Delta^2-5)\tilde{\eta}_{x_m,y_n}$$
$$+\frac{4}{3}\tilde{\eta}_{x_{m+1},y_n}+\frac{4}{3}\tilde{\eta}_{x_m,y_{n+1}}-\frac{1}{12}\tilde{\eta}_{x_{m+2},y_n}-\frac{1}{12}\tilde{\eta}_{x_m,y_{n+2}}=0. \quad (2.18)$$

Furthermore, near the boundaries (one grid inward off the boundary), a different stencil is required as Eq. (2.18) will not fit here. The formulation for the West Near-Boundary is given below with its corresponding stencil in Figure 2.2b. The stencil can be flipped and/or rotated without changing the sign of the coefficients to obtain the formulation for the other near-boundary grid nodes.

$$-\frac{1}{12}\tilde{\eta}_{x_m,y_{n-2}}+\frac{4}{3}\tilde{\eta}_{x_m,y_{n-1}}+\frac{10}{12}\tilde{\eta}_{x_{m-1},y_n}-\left(K^2_{x_m,y_n}\Delta^2-\frac{15}{12}-\frac{5}{2}\right)\tilde{\eta}_{x_m,y_n}-\frac{4}{12}\tilde{\eta}_{x_{m+1},y_n}$$
$$+\frac{14}{12}\tilde{\eta}_{x_{m+2},y_n}-\frac{6}{12}\tilde{\eta}_{x_{m+3},y_n}+\frac{1}{12}\tilde{\eta}_{x_{m+4},y_n}+\frac{4}{3}\tilde{\eta}_{x_m,y_{n+1}}-\frac{1}{12}\tilde{\eta}_{x_m,y_{n+2}}=0. \quad (2.19)$$

The discretized boundary conditions are formulated as follows:

$$\tilde{\eta}_{x_1,y_n}=\tilde{A} \qquad \text{at}\Gamma_{\text{west}}, \quad (2.20)$$

$$\frac{25}{12}\tilde{\eta}_{x_m,y_N}-4\tilde{\eta}_{x_m,y_{N-1}}+3\tilde{\eta}_{x_m,y_{N-2}}-\frac{4}{3}\tilde{\eta}_{x_m,y_{N-3}}+\frac{1}{4}\tilde{\eta}_{x_m,y_{N-4}}=0 \qquad \text{at}\Gamma_{\text{north}}, \quad (2.21)$$

$$\left(\frac{25}{12}-iK_{x_m,y_n}\Delta\right)\tilde{\eta}_{x_N,y_n}-4\tilde{\eta}_{x_{N-1},y_n}+3\tilde{\eta}_{x_{N-2},y_n}-\frac{4}{3}\tilde{\eta}_{x_{N-3},y_n}+\frac{1}{4}\tilde{\eta}_{x_{N-4},y_n}=0 \qquad \text{at}\Gamma_{\text{east}}, \quad (2.22)$$

$$-\frac{25}{12}\tilde{\eta}_{x_m,y_1}+4\tilde{\eta}_{x_m,y_2}-3\tilde{\eta}_{x_m,y_3}+\frac{4}{3}\tilde{\eta}_{x_m,y_4}-\frac{1}{4}\tilde{\eta}_{x_m,y_5}=0 \qquad \text{at}\Gamma_{\text{south}}. \quad (2.23)$$

Furthermore, the stencils belonging to the boundary conditions given in Eq. (2.9)-(2.11) are depicted in Figure 2.2c. Lastly, there are also corner nodes one grid inward off the boundary which require formulation. These corner nodes are a combination of Eq. (2.14) and (2.15).

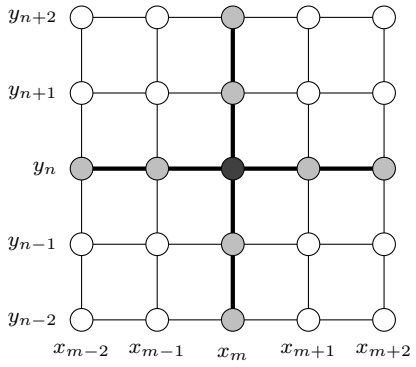

(a) The central spaced stencil for the interior nodes in the domain as given in (2.18).

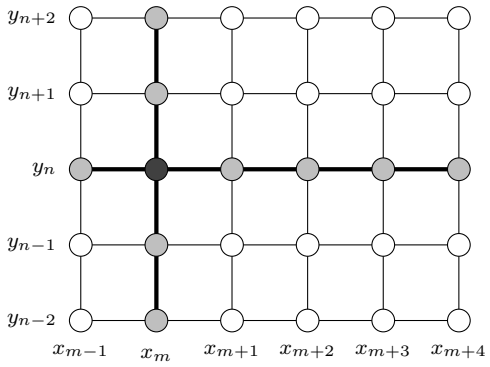

(b) Stencil representing the in x direction off-centered discretized model equation on the West Near-Boundary grid nodes as given in Eq. (2.19). The stencil can be rotated and flipped to obtain the North, West and South Near-Boundary Stencil.

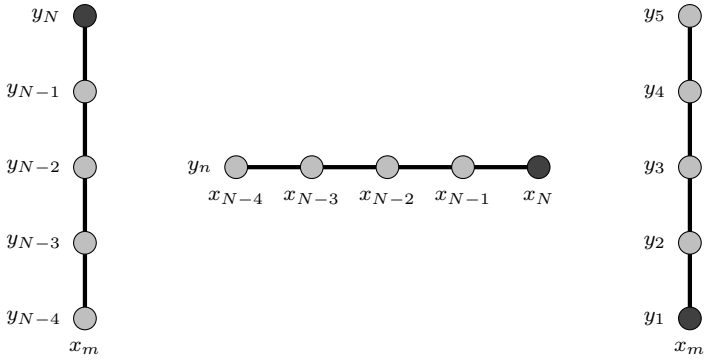

(c) From left to right: stencils corresponding to North, East and South Boundary grid nodes, represented by a one-sided finite difference as given in Eq. (2.21)-(2.23).

Figure 2.2: Visualization of the fourth order accurate stencils used for the model formulation. The dark shaded node is the evaluated grid node (or base point), the light shaded nodes are used to formulate the base point.

2.4 Direct solution method

In order to obtain a solution, the linear system of equation resulting from the discretizations presented in Section 2.3, it is chosen to use a Direct Solution Method. Therefore the unknowns at each grid node are expressed in matrix notation as follows

$$[V]\{\tilde{\eta}\} = \{f\}, \tag{2.24}$$

where $[V]$ is the system matrix, $\{\tilde{\eta}\}$ is the unknown vector of complex valued amplitudes and $\{f\}$ is a vector containing the known right hand side of the discretized equations. The unknown vector matrix $\{\tilde{\eta}\}$ can then be obtained by computing the inverse of $[V]$ as given in the following expression:

$$\{\tilde{\eta}\} = [V]^{-1}\{f\}. \tag{2.25}$$

In MATLAB, the operation in Eq. (2.25) is extensive and therefore it is more convenient to use the build-in solver for systems of linear equations (i.e. backslash operator). It uses the optimal solve technique corresponding to the structure of the matrix. The function should look like: $\{\tilde{\eta}\} = [V]\backslash\{f\}$. Furthermore, the *sparse* identity of the system matrix is used in our advantage such that RAM requirements are reduced to manageable proportions. A more detailed explanation on this sparse implementation is given in Appendix A.2.

2.5 Model verification

In order to assess the accuracy of the model, we choose to verify the numerical solution in a flat-bed situation for which an analytical solution exists. The error is quantified with the scaled Root-Mean-Square Error (RMSE) and is defined as follows:

$$\text{RMSE} = \frac{1}{A_0}\sqrt{\frac{1}{N^2}\sum_{n=1}^{N}\sum_{m=1}^{N}\left|\hat{\eta}_{m,n} - \hat{\eta}_{A_{m,n}}\right|^2}, \tag{2.26}$$

where A_0 is the amplitude of the predefined incident wind wave, N^2 is the number of grid nodes, $\hat{\eta}$ is the numerical solution of the complex valued amplitude and $\hat{\eta}_A$ is the analytical solution of the complex valued amplitude. The analytical solution is given by:

$$\hat{\eta}_A(x, y) = A_0 e^{ik_0 x}, \tag{2.27}$$

where i is the imaginary unit and k_0 is the constant wave number according to the dispersion relationship in Eq. (1.2).

The differences between the analytical and numerical solution are visualised in Figure 2.3. From this surface plot it can be seen that the differences of the real and imaginary parts are uniform in y-direction, which is in coherence with expectation based on symmetry. Although it is hard to notice in Figure 2.3a, the error increases when x increases (the trough is less deep than the crest is high), this is caused by a dispersion error.

Furthermore, in Figure 2.4 RMSE is plotted against the number of grid nodes in one direction N. Here it can be seen that the RMSE of the fourth order accurate model decreases fourth order with respect to the increasing number of grid nodes. Also, in Figure 2.4, the second order model is included which shows a second order decrease (see Appendix A.3). When comparing these two discretizations, it can be seen that the error of the fourth order discretization reduces faster with an increasing number of grid nodes. Therefore, less grid nodes are required to obtain the same accuracy which reduces the computational cost to manageable proportions for a personal computer.

In Figure 2.5 different combinations of the wave number k and the step size Δ are assessed and the RMSE error is determined. $k\Delta$ is a dimensionless number to express the number of grid nodes per wave length (points per wave length is $2\pi/(k\Delta)$). The restriction of RAM storage required that the maximum allowed RMSE is set to 10^{-2}, the value of $k\Delta$ should then be less than about 0.5 [-].

Based on the limitations of RAM storage and accuracy, a domain is chosen of $5,000$ by $5,000$ meter with a step size Δ of 5 meter. This results in a grid of $1,000$ by $1,000$ nodes, and a system matrix that can be solved on a 64-bit system with 8 Gigabyte RAM. Furthermore, the threshold of a maximum RSME of 10^{-2} in combination with $\Delta = 5$ [m], requires that the wave numbers k inside the system may not exceed a value of 0.125 $[m^{-1}]$. The latter corresponds with wave lengths of more than about 60 meter.

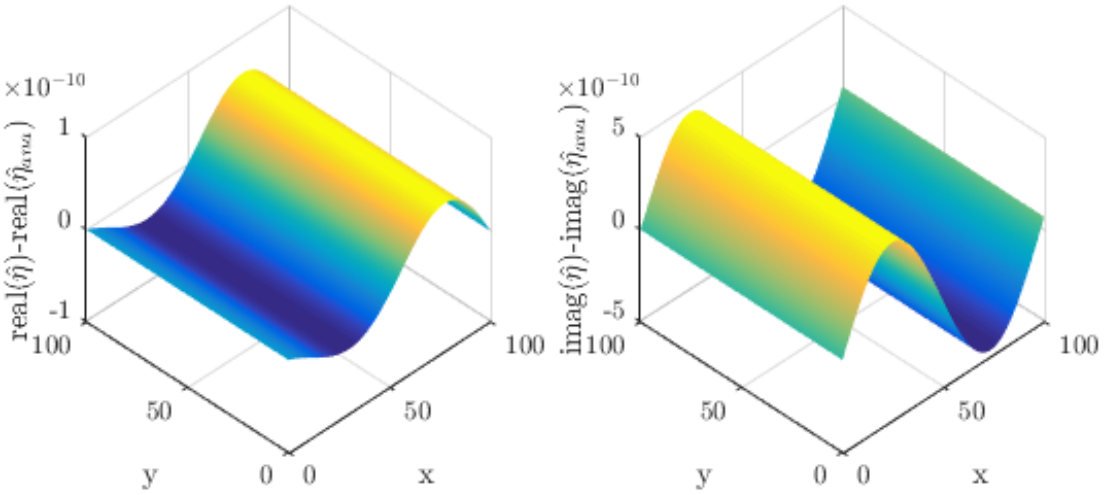

(a) Difference of real parts $\Re\{\hat{\eta}\} - \Re\{\hat{\eta_A}\}$ **(b)** Difference of imaginary parts $\Im\{\hat{\eta}\} - \Im\{\hat{\eta_A}\}$

Figure 2.3: Surface plots of the difference between the numerical and analytical solution. Domain is 100 by 100 [m], $k_0 = 0.063$ $[m^{-1}]$, $\Delta = 0.1$ [m]. Differences are in the order of 10^{-10}.

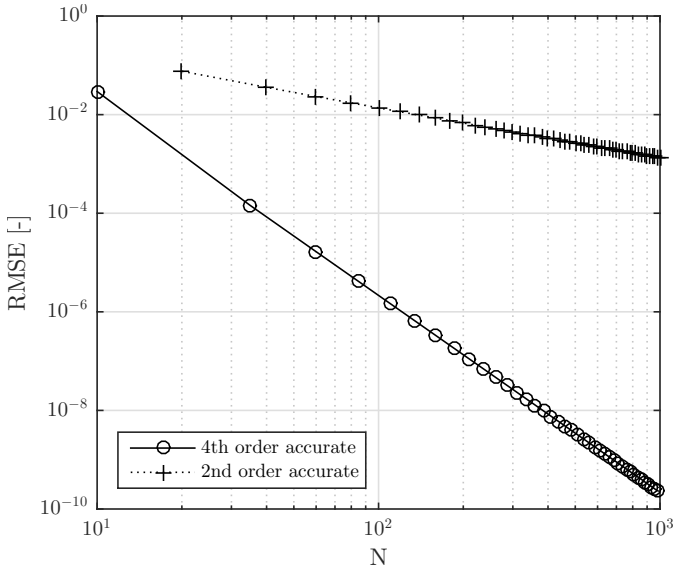

Figure 2.4: Increasing number of grid nodes N in x-direction (or y) versus RMSE. The domain size used for this verification was 100 by 100 [m].

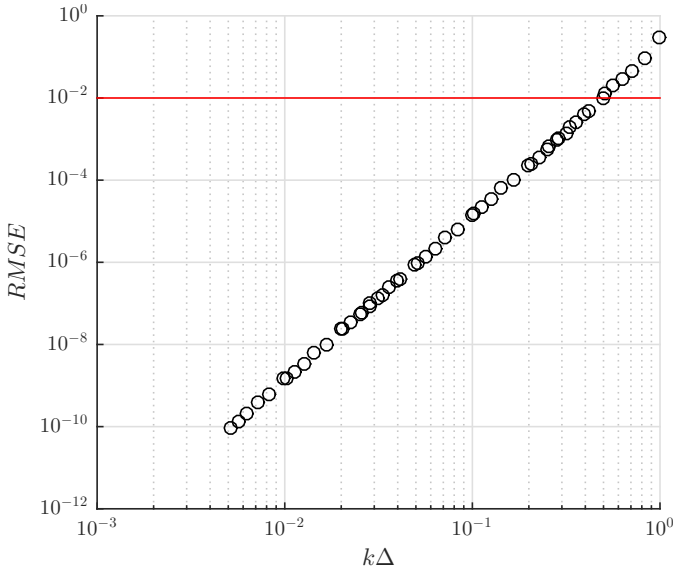

Figure 2.5: different combinations of $k\Delta$ versus RMSE on a domain size of 100 by 100 [m]. With a threshold (indicated with the red horizontal line) set to RMSE = 10^{-2}, the $k\Delta$ should be less than about 0.5.

Chapter 3

Bathymetry generation

3.1 Introduction

The model formulated in the previous section requires the variable water depth $h(x, y)$ between the still water level ($\eta = 0$) and the bed as input. To assess an arbitrary, regular sand wave field pattern, in this chapter a two-dimensional bed elevation function is formulated that describes the bathymetry $z_b(x, y)$ of a sand wave field. This bathymetric function allows for variation in the characteristics given below, which are also visualized in Figure 3.1.

- Sand wave height, denoted as H_b, is the vertical distance between the trough and crest of a sand wave.
- Sand wave length, denoted as λ_b is the horizontal distance between the troughs of a sand wave.

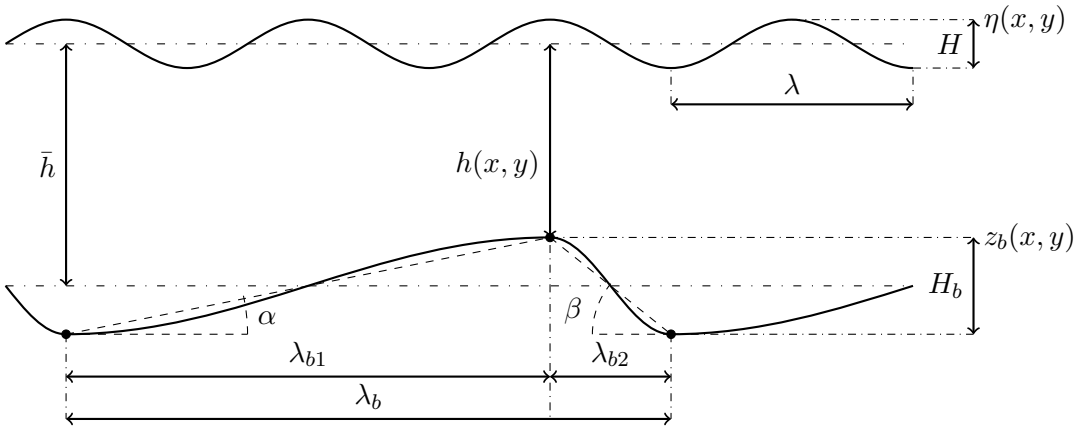

Figure 3.1: The cross-section of a (asymmetric) sandwave with corresponding nomenclature.

- Asymmetry, denoted as S_b is the ratio between the length of the stoss λ_{b1} and lee λ_{b2} side and is expressed as:

$$S_b = \frac{\lambda_{b1}}{\lambda_{b2}}. \tag{3.1}$$

  Stoss is here defined as the slope that faces the incident wind wave and lee is the shadow zone with respect to the wind wave. The asymmetry factor can be classified as follows:

  - when $S_b < 1$, the stoss side is steeper than the lee side;
  - when $S_b = 1$, the wave is symmetric;
  - when $S_b > 1$, the lee side is steeper than the stoss side.

- Orientation, denoted as θ_b is the orientation angle of the sand wave crests with respect to the crests of the incident wind wave (or for our model also with respect to the y axis).

- Undisturbed water depth, denoted as $\bar{h}$, is the water depth between the still water level ($\eta = 0$) and the flat bed ($z_b = 0$).

Below, a step by step explanation is given about how these characteristics are included in a comprehensive 2D bed elevation function. Therefore, in Section 3.2, is explained how the sand wave field can be represented by a plane wave. Then, in Section 3.3, asymmetry of the sand wave profile is included. Finally, in Section 3.4, a tapering function is introduced required to generate the sand wave field patch surrounded by a flat-bed configuration towards the boundaries of the domain.

3.2 Plane wave with arbitrary wave length, wave height and orientation

A plane wave is a wave of constant wave number and amplitude with infinitely long wave fronts. It can be used to represent the bed elevation z_b of a sand wave field within a given domain. Due to very slow displacement rates of sand waves, the waves are assumed to be static and therefore time-dependency is neglected. Then, when considering a two dimensional horizontal domain (x, y), the bed elevation for an arbitrary orientation θ_b can be expressed as follows:

$$z_b(x, y) = A_b \cos(k_{bx}x + k_{by}y), \tag{3.2}$$

with

$$\lambda_b = \frac{2\pi}{\sqrt{k_{bx}^2 + k_{by}^2}}, \qquad \theta_b = \arctan\left(\frac{k_{by}}{k_{bx}}\right). \tag{3.3}$$

where $A_b = H_b/2$ is the amplitude of the sand wave, λ_b is the sand wave length, k_{bx} and k_{by} are the counterparts of the wave vector $|\vec{k_b}| = 2\pi/\lambda_b$ in x and y direction respectively,

and θ_b is the angle in degrees of the wave front with respect to the y-axis. Subsequently, the variable water depth from the still water level ($\eta = 0$) to the undulating bed, can be calculated as follows

$$h(x, y) = \bar{h} - z_b(x, y), \tag{3.4}$$

where $\bar{h}$ is the undisturbed water depth. Example plots of $h(x, y)$, with orientations of 0 and 60 degrees, are depicted in 3.2a and 3.2b, respectively.

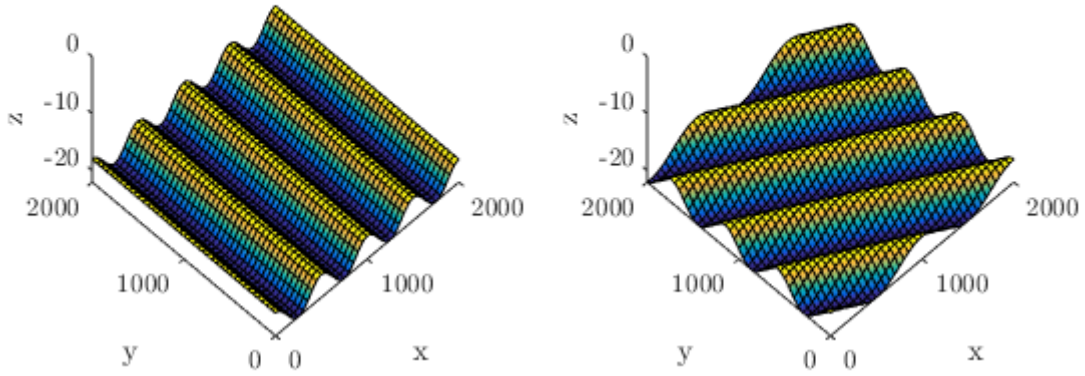

(a) $h(x, y)$, $\theta_b = 0$. **(b)** $h(x, y)$, with $\theta_b = 60°$.

Figure 3.2: Example surface plots of the bathymetry represented by a plane wave when including (a) no orientation and (b) orientation. Both panels are characterized by $H_b = 4$ [m], $\bar{h} = 20$ [m] and $\lambda_b = 500$ [m].

3.3 Asymmetry

In order to describe a smooth asymmetric profile two sinusoids, with different wave numbers for the stoss and lee side, are merged together. This requires introduction of the factor γ_{stoss} and γ_{lee} which, when multiplied with k_{bx} or k_{by}, will result in the appropriate wave number for the stoss and lee side. The bed elevation including asymmetry can then be expressed as follows:

$$z_b(x, y) = \begin{cases} A_b \cos\left(\gamma_{\text{lee}}\left[k_{bx}x + k_{by}y - \varphi_1\right]\right), & \text{if } \varphi_1 \leq k_{bx}x + k_{by}y < \varphi_2 \\ A_b \cos\left(\gamma_{\text{stoss}}\left[k_{bx}x + k_{by}y - \varphi_2\right] + \pi\right), & \text{if } \varphi_2 \leq k_{bx}x + k_{by}y < 2\pi(p+1) \end{cases}, \tag{3.5}$$

where

$$\varphi_1 = 2\pi p, \qquad \varphi_2 = 2\pi\left(p + \frac{1}{2\gamma_{\text{lee}}}\right), \qquad p = \left\lfloor \frac{k_{bx}x + k_{by}y}{2\pi} \right\rfloor, \qquad p \in \mathbb{Z}. \tag{3.6}$$

In Eq. (3.5) and (3.6) φ_1 is the phase where cycle p starts and the lee side begins (crest) and φ_2 is the position inside cycle p where the stoss side begins (trough). At a local position (x, y) the cycle number p can be determined with the *floor* function as indicated in the third term of Eq. (3.6). The factor γ_{stoss} and γ_{lee} can be determined with the asymmetry factor S_b as given in Eq. 3.1 as follows:

$$\gamma_{\text{stoss}} = S_b \gamma_{\text{lee}} = \left(\frac{1 + S_b}{2S_b} \right). \tag{3.7}$$

Please note that for orientations $\theta_b > 90°$, the latter formulation will flip the steep and mild sides due to the definition of the stoss side being the side that faces that the incident wind wave. The derivation of Eq. (3.7) can be found in Appendix A.4. After calculating the bed elevation, Eq. (3.4) can be used to compute the variable water depth which is required for our model. An example plot of a bathymetry including asymmetry is given in Figure 3.3.

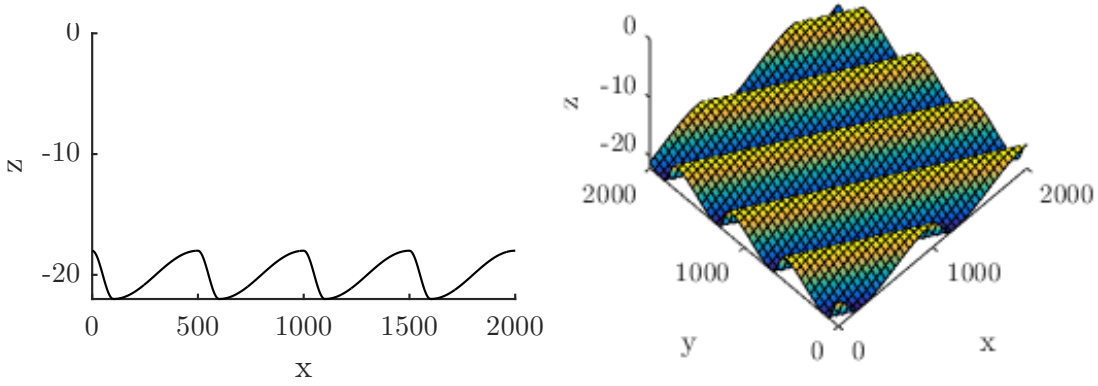

(a) 1D, $z(x)$, with $S_b = 4$.

(b) 2D, $z(x, y)$, with $\theta_b = 60°$ and $S = 4$.

Figure 3.3: Example plots of a bathymetry including an asymmetric sand wave profile. Both panels are characterized by $H_b = 4$ [m], $\bar{h} = 20$ [m] and $\lambda_b = 400$ [m].

3.4 Tapering function

A tapering function is used to create a patch-like sand wave field with a flat-bed configuration surrounding it. This is done to minimize undesired interference of the wind waves with the boundary. This tapering function $w_{2D}(x, y)$ describes a trapezium shaped function with values ranging from zero to one. This tapering function will be multiplied with the bed elevation $z_b(x, y)$ to create the desired flat-bed configuration towards the boundaries.

The domain can be divided into three zones as can be seen in Figure 3.4. The outer zone Ω_0 is the flat-bed zone, here the tapering function needs to describe zero-values. The middle zone Ω_1 consists of two parts, Ω_{1t} and Ω_{1s}. Ω_{1t} is a transition zone which gently introduces the sand wave field, here the tapering function requires to describe a linear slope between zero and one. Ω_{1s} is the sand wave field, here the tapering function needs to describe one-values. When adding the transition and inner zone ($\Omega_{1t} \cup \Omega_{1s}$), one obtains Ω_1 as indicated in Figure 2.1.

In order to divide the domain into these three zones, two input parameters are defined, namely γ_0 and γ_t, which represent the ratio of the domain used for respectively the flat-bed zone and transition zone. From the relations in Figure 3.4 can be seen that the condition

$$\gamma_0 + \gamma_t < 0.5, \tag{3.8}$$

must be satisfied to ensure a feasible distribution of the zones. The tapering function in x and y direction only can then be determined with

$$w(s) = \begin{cases} 0, & \text{if } P \geq s \geq S \\ (\gamma_t L)^{-1}(s - P), & \text{if } P < s \leq Q \\ 1 - (\gamma_t L)^{-1}(s - R), & \text{if } R \leq s < S \\ 1, & \text{if } Q < s < R \end{cases}, \tag{3.9}$$

where L the width of the square domain, and P, Q, R and S represent points for which the dimensions can be obtained from Figure 3.4. Subsequently the tapering function for the two dimensional domain can then be obtained by

$$w_{2D}(x, y) = w(x)w(y), \tag{3.10}$$

for which $w(x)$ and $w(y)$ are determined with Eq. (3.9). Example plots of the 1D and 2D tapering function are depicted in Figure 3.5.

When multiplying $w(x, y)$ with the bed elevation $z_b(x, y)$ and subsequently subtracting this from the undisturbed water depth $\bar{h}$, one obtains the variable water depth, which is expressed as follows:

$$h(x, y) = \bar{h} - w_{2D} z_b(x, y), \tag{3.11}$$

A surface plot of the bathymetry including orientation, asymmetry and a tapering function to create the patch-like sand wave field is given in Figure 3.5c.

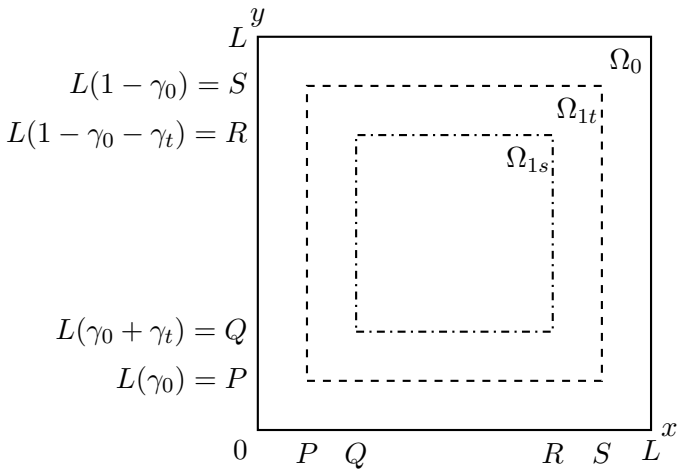

Figure 3.4: Sketch of the square domain of length L in both x and y direction including nomenclature for the tapering function. Ω_0 is the flat bed zone, Ω_{1t} is the transition zone, and Ω_{1s} the sand wave field zone ($\Omega_1 = \Omega_{1t} \cup \Omega_{1s}$). Furthermore, P, Q, R, S are points.

(a) Example of 1D tapering function $w(s)$

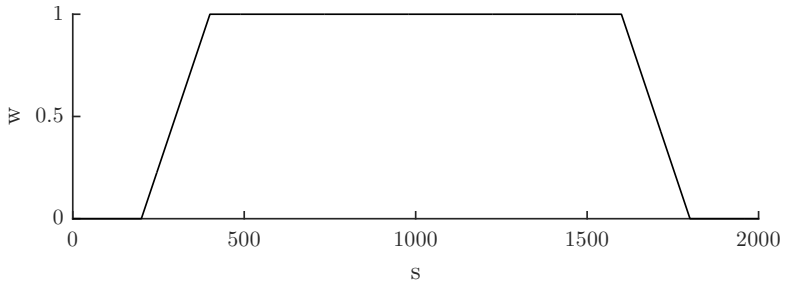

(b) Example of 2D tapering function $w_{2D}(x, y)$

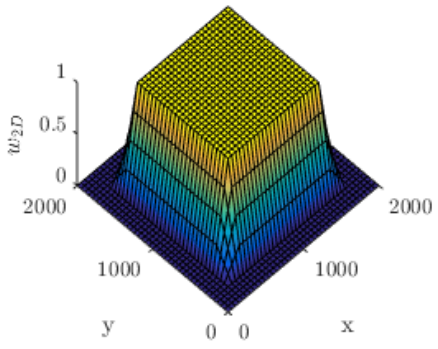

(c) 2D tapering function applied on a sand wave field

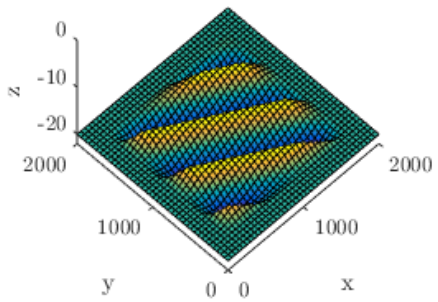

Figure 3.5: Example surface plot of both the tapering function itself and applied on a sand wave field.

Chapter 4

Results

4.1 Introduction

By inserting the bathymetric data as explained in Chapter 3 in the model and formulating the configuration of the incident wind wave, the model outputs the simulated complex valued amplitudes $\hat{\eta}$ in the domain. Due to the varying bathymetry, the complex valued amplitudes will show spatial variability. In this Chapter this spatial variability is visualized and quantified.

In order to present an unambiguous view of the spatial variability of the wind waves caused by the sand wave field, and hence not by phase differences of the wind wave, it is chosen to transform the model output by first taking the absolute of the complex valued amplitude: $|\hat{\eta}|$. This essentially tells us the local amplitude of the wind wave. Subsequently, the dimensionless Amplification Factors AF_A of the local wind wave amplitudes can be calculated as follows:

$$\mathrm{AF}_A(x,y) = \frac{|\hat{\eta}|(x,y)}{A_0}, \tag{4.1}$$

where A_0 is the predefined amplitude of the incident wind wave at the West boundary. When for example locally an amplification factor of 2 is found, the local amplitude is twice the amplitude of the incident wind wave. These Amplification Factors are used to visualize and quantify the spatial variability.

Furthermore, due to the potential interest to the near-bed influence of wind waves, also the spatial variability of the near-bed orbital velocities is visualized and quantified. In order to transform the complex valued amplitude to near-bed orbital velocities the complex velocity potential is used (see Eq. (2.6)). Furthermore, also here is chosen to exclude spatial variability caused by phase differences of the wind wave. The latter is done by using the local near-bed orbital velocity amplitudes:

$$|\hat{u}_{\mathrm{nb}}|(x,y,z) = \left|\frac{d\hat{\Phi}}{dx}\right|_{z=-h} \qquad |\hat{v}_{\mathrm{nb}}|(x,y,z) = \left|\frac{d\hat{\Phi}}{dy}\right|_{z=-h}, \tag{4.2}$$

where $|\hat{u}_{\mathrm{nb}}|$ and $|\hat{v}_{\mathrm{nb}}|$ are the near-bed orbital velocity amplitudes in respectively x and y direction and $\hat{\Phi}$ is the complex flow potential as given in Eq. (2.6). Subsequently, an amplification factor is used to express the amplification with respect to the near-bed orbital velocity at the west boundary. The amplification Factor of the near-bed flow velocity amplitude $\mathrm{AF}_{\mathrm{nb}}$ is expressed as:

$$\mathrm{AF}_{\mathrm{nb}} = \frac{|\vec{u}_{\mathrm{nb}}|}{|\vec{u}_{\mathrm{nb,west}}|}, \qquad |\vec{u}_{\mathrm{nb}}| = \sqrt{|\hat{u}_{\mathrm{nb}}|^2 + |\hat{v}_{\mathrm{nb}}|^2}, \tag{4.3}$$

where $|\vec{u}_{\mathrm{nb}}|$ is the magnitude of the near-bed orbital flow velocity amplitude vector and $|\vec{u}_{\mathrm{nb,west}}|$ is the the near-bed orbital flow velocity amplitude at the (flat-bed) west boundary Γ_{west}.

Lastly in Appendix B the $\sinh(kh)$ values are visualized. The latter gives an impression of the influence of the bathymetry on the near-bed velocities assuming a still water level, i.e. excluding the influence exerted by an increasing or decreasing wind wave amplitude.

4.2 Visualization of model output

4.2.1 Visualization method

To visualize the spatial variability of the amplification of wind wave amplitude AF_{A} and near-bed orbital flow velocity $\mathrm{AF}_{\mathrm{nb}}$, it is chosen to create a top-view plot of the domain where a colormap is used to distinct between high and low values. A bright, yellow color indicates high values whereas a dark, blue color indicates low values. Further, to prevent visualization (and later on quantification) of distortion due to the transition from flat-bed configuration to sand wave field, there is chosen to visualize only the part of the domain as indicated with the solid line in Figure 4.1. A size of 2000 by 2000 meter is chosen for this area of interest such that still two sand waves with a wave length of 1000 meter are able to be positioned inside this area.

To explore the influence of the parameters on spatial variability, a base configuration is formulated and from there, the parameters are changed individually. By trial-and-error the base case is chosen with the sand wave crests perpendicular to the incident wind wave crests, as this case showed the highest influence of other parameters. The influence of changing the wind wave amplitude is not shown, as it will not influence spatial variability. Several visualizations are made, for which a summary of the parameter configurations is given in Table 4.1.

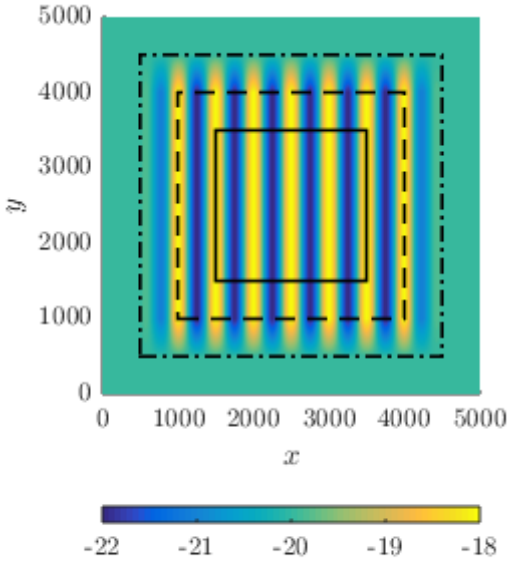

Figure 4.1: Definition of area of interest, the dash-dotted line is where the transition starts from flat-bed configuration to sand wave field, the dashed line is where the sand wave field patch is fully developed and the solid line represent the area of interest.

Fig.	Description	θ_b [deg]	$\bar{h}$ [m]	λ_b [m]	H_b [m]	S_b [-]	T [s]	A_0 [m]
4.2	base case	90	20	500	4	1	9	2
4.3	parallel orientation	0	20	500	4	1	9	2
4.4	shallower	90	12	500	4	1	9	2
4.5	longer sand waves	90	20	1000	4	1	9	2
4.6	lower sand waves	90	20	500	2	1	9	2
4.7	asymmetry	90	20	500	4	5	9	2
4.8	shorter wave period	90	20	500	4	1	7	2

Table 4.1: Overview of parameter configurations underlying the top-view visualization figures representing spatial variability.

4.2.2 Sand wave orientation

Spatial variability is dominantly influenced by the orientation θ_b of the sand wave field. In Figure 4.2 and 4.3 the spatial variability is visualized for $\theta_b = 90°$ and $\theta_b = 0°$ respectively. These specific orientations are chosen to compare a high-influence and low-influence sand wave field configuration, respectively. In both Figures, panel (a) shows the local water depth, (b) the amplification of the wind wave amplitude and (c) the amplification of the near-bed orbital flow velocity.

In Figure 4.2b, above the sand wave crests, zones of amplification are visible indicating spatial variability whereas Figure 4.3b shows insignificant amplification of the wind wave amplitude. Zones of amplification indicate shoaling of the wind waves. Also, in figure 4.2b, minor amplifications are visible above the crests around $x = 3000$ meter.

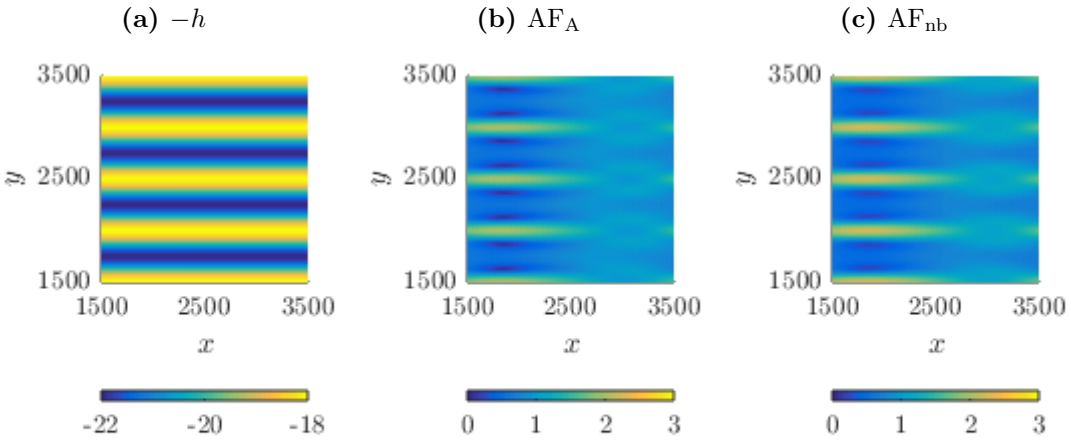

Figure 4.2: Visualization of the spatial variability of the base case. For parameter configuration see Table 4.1. (a) shows the local water depth, (b) the amplification of the wind wave amplitude, (c) the amplification of the near-bed flow velocity.

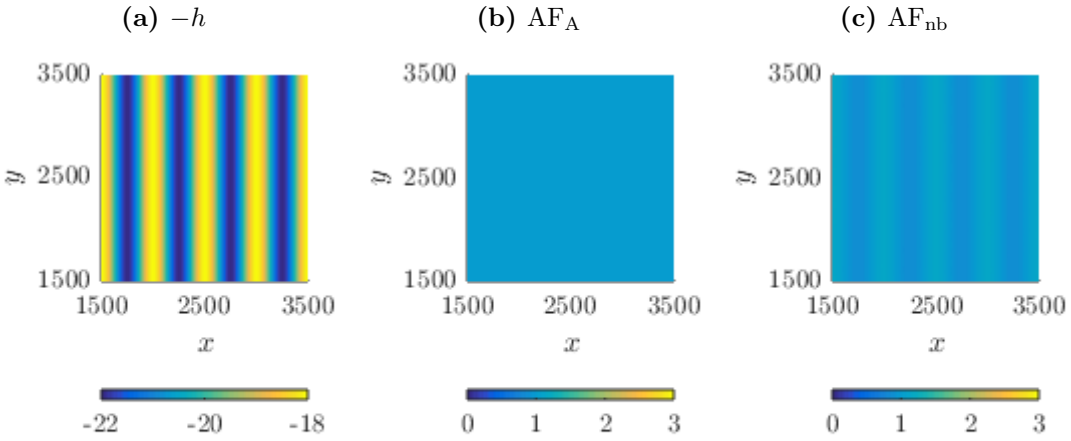

Figure 4.3: Visualization of the spatial variability with the sand wave crests oriented parallel to the wind wave crests. For parameter configuration see Table 4.1. (a) shows the local water depth, (b) the amplification of the wind wave amplitude, (c) the amplification of the near-bed flow velocity.

Furthermore in Figure 4.2c, the amplification of the near-bed flow velocity shows similar patterns to that of AF_A. In Figure 4.3c only minor amplification of near-bed orbital flow is visible.

In Figure B.1 and B.2 a visualization of $\sinh(kh)$ is given. For both figures an increase of $\sinh(kh)$ is noticeable above the sand wave crests.

Furthermore, other visualizations showed that hardly any spatial variability was visible for sand wave field orientations between 0 and about 55 degrees. In case of orientation angles larger than 55 degrees, the spatial variability started to increase significantly.

4.2.3 Mean water depth

When the mean water depth $\bar{h}$ decreases, higher amplifications and near-bed flow velocities are found. In Figure 4.4 the base case is changed to a depth of 12 meter. In Figure 4.4b it is visible that zones of amplification occur above the sand wave crests indicating the process of shoaling. In comparison to the base case, these shoaling zones are more compact and show higher amplifications. Possibly, due to a smaller water depth, the process of refraction of the wind waves is stronger, such that more compact zones of amplification are visible.

Furthermore, in Figure 4.4c, the amplification of near-bed velocity is depicted. Similar patterns to that of AF_A are visible. The zones of amplification of near-bed flow above the sand wave crests are slightly wider in x and y direction than that of AF_A.

In Figure B.3 a visualization of $\sinh(kh)$ is given. This figure shows that $\sinh(kh)$ decreases when water depth becomes smaller. Also, the difference between the values above the crests and troughs becomes more evident.

Lastly, when assessing an increase of water depth, the zones of amplification stretch out in x direction and become less apparent, possibly because the process of refraction is now weaker.

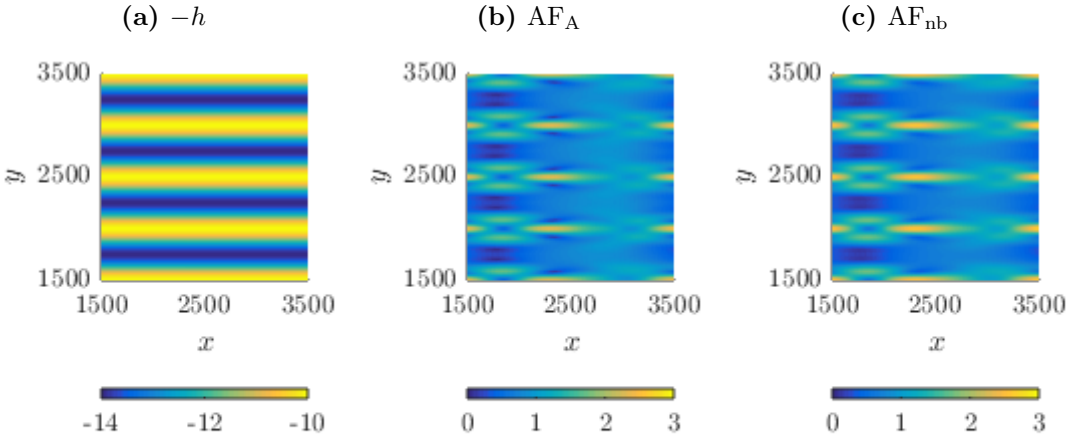

Figure 4.4: Visualization of the spatial variability in case of a reduction in water depth. For parameter configuration see Table 4.1. (a) shows the local water depth, (b) the amplification of the wind wave amplitude, (c) the amplification of the near-bed flow velocity.

4.2.4 Sand wave length

To assess what happens to wind waves when the sand wave length increases, Figure 4.5 shows the base case now with a sand wave length of 1000 meter. In Figure 4.5b it can be seen that the amplification zones are more concentrated than in the base case indicating stronger shoaling and refraction effects.

In Figure 4.5c the amplification of near-bed flow velocity is depicted. Similar patterns are found to that of AF_A. Hence, the highest orbital velocities are found above the sand

wave crests. In Figure B.4 a visualization of $\sinh(kh)$ is given. Due to the longer slopes of the sand waves, the transition of relatively high $\sinh(kh)$ values at the crests to relatively low $\sinh(kh)$ values in the trough is more gentle.

Lastly, when sand wave length decreases, the zones of amplification become less apparent and will extend in x direction. This means that wind wave amplitudes will become less high and more spread over the sand wave crests.

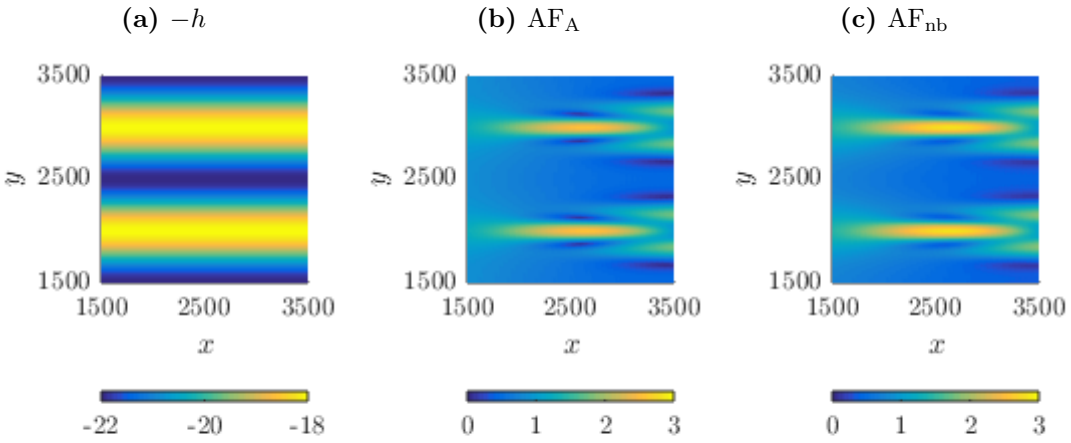

Figure 4.5: Visualization of the spatial variability in case of a longer sand waves. For parameter configuration see Table 4.1. (a) shows the local water depth, (b) the amplification of the wind wave amplitude, (c) the amplification of the near-bed flow velocity.

4.2.5 Sand wave height

In Figure 4.6 the influence of sand wave height is assessed by adjusting the base case to a lower sand wave height of 2 meter.

Figure 4.6b shows the amplification factors of the wind wave amplitude. It is visible that that zones of amplification occur above the sand wave crest which have roughly the same magnitude as in the base case. The sand wave slopes are less steep and therefore the wind wave crests require a longer distance to bend, resulting in a more extended amplification zone in x direction.

In Figure 4.6c the amplification of the near-bed velocity is depicted. It shows similar patterns as that of AF_A. Also here, the zones of amplification are extended in x direction. The $\sinh(kh)$ visualization in Figure B.5 shows highest values above the sand wave crests. Compared to the base case the difference between the values above the crests and troughs has become less apparent.

Lastly, when assessing a larger sand wave height, roughly the same patterns are found as in the base case (Figure 4.2), only now the depression (at about $x = 3000$ [m] in Figure 4.2) of the amplification zones is shifted to the left. Due to steeper slopes in this situation, the wind waves require less distance to bend towards the sand wave crests. Furthermore, slightly higher magnitudes are found in amplification factors and

near-bed orbital velocities.

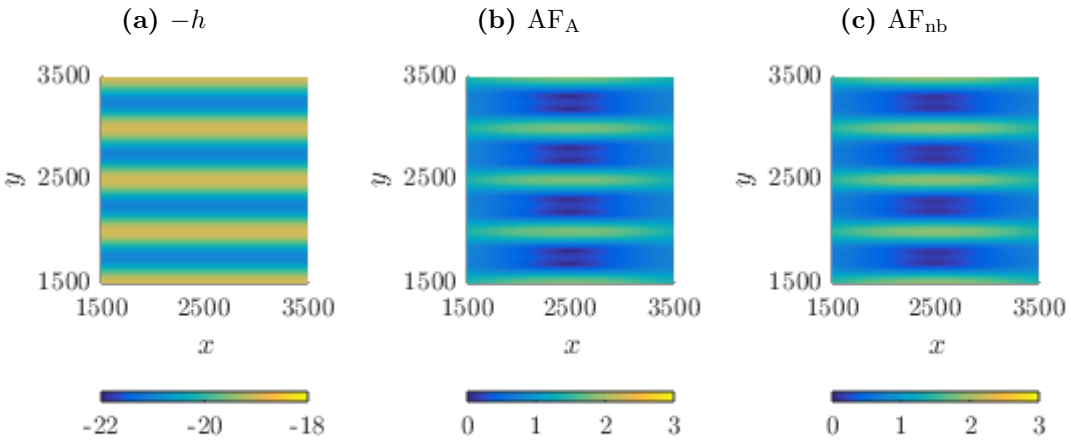

Figure 4.6: Visualization of the spatial variability in case of lower sand waves. For parameter configuration see Table 4.1. (a) shows the local water depth, (b) the amplification of the wind wave amplitude, (c) the amplification of the near-bed flow velocity.

4.2.6 Asymmetry

The base case in Figure 4.2, is configured with perfectly symmetric sand waves. To assess the influence of asymmetry, there is chosen to change the base case with an asymmetry factor S_b of 3, which means that the longest sides of the sand waves are three times as long as the short sides. The latter is visualized in Figure 4.7.

In Figure 4.7b it can be seen that asymmetry causes that the zones of amplification show some sort of curvature towards the steep side of the sand wave. When x increases, the zones of amplification become less apparent. Apparently, the wind waves shoal higher at the west than at the east and they progressively move towards the steep side of the sand wave. Furthermore, it seems that the patterns are still in a build-up phase. Likely, a repeating pattern will result when a larger domain is chosen.

In Figure 4.7c the amplification of the near-bed orbital velocity is depicted. Similar patterns are found as that of AF_A. Compared to the base case relatively same magnitudes are found however the depression in amplification in the base case (i.e. roughly at $x = 3000$ meter) is now not so apparent.

When looking at the $\sinh(kh)$ values in Figure B.6, it can be seen that a different gradient is visible in $\sinh(kh)$ above the steep and mild slope of the sand wave.

4.2.7 Wave period

To visualize the influence of a changing wind wave period, Figure 4.8 shows the base case now with a wind wave period of 7 seconds. In case of a shorter wind wave period, only minor influences are visible in the magnitudes of amplification factors and near bed

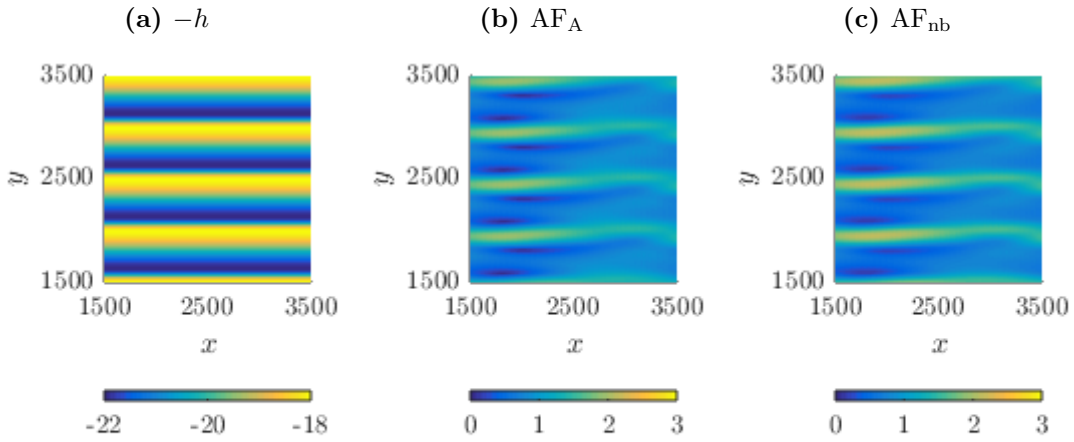

Figure 4.7: Visualization of the spatial variability in case of asymmetric sand waves where the longest side is three times as long as the short side. For parameter configuration see Table 4.1. (a) shows the local water depth, (b) the amplification of the wind wave amplitude, (c) the amplification of the near-bed flow velocity.

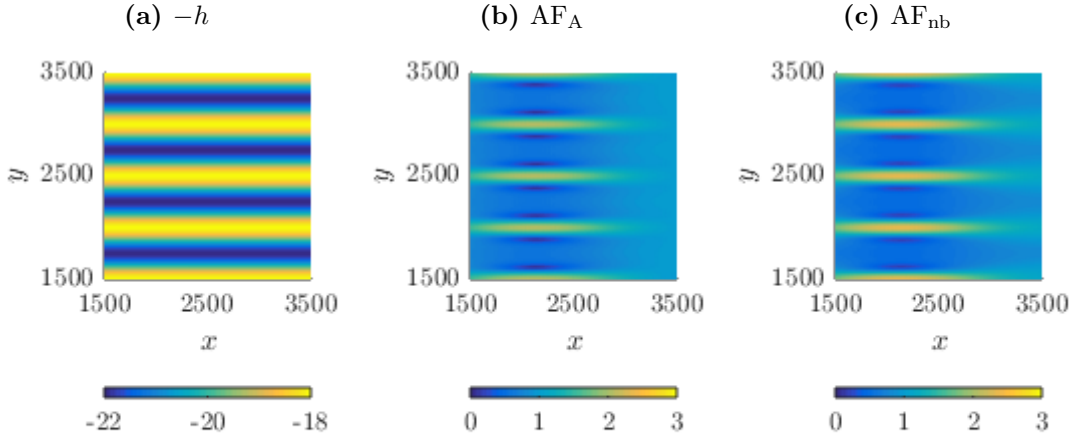

Figure 4.8: Visualization of the spatial variability in case of a shorter wind wave period. For parameter configuration see Table 4.1. (a) shows the local water depth, (b) the amplification of the wind wave amplitude, (c) the amplification of the near-bed flow velocity.

flow velocities. The shoaling zones above the sand wave crests as can be seen in Figure 4.8b extend in x direction, which is also the case for the amplification of the near-bed flow velocities in Figure 4.8c.

In Figure B.7 the spatial variability of $\sinh(kh)$ is visualized. Apparently, due to the shorter wave period the $\sinh(kh)$ values increase significantly. Therefore the influence of the bathymetry only (i.e. without the influence caused by increase or decrease of wind wave amplitude) on the near-bed velocities becomes stronger.

In case of an increasing wind wave period the spatial influences become even smaller.

Also here, still the same magnitudes are found for amplification factors of wind wave amplitudes and near-bed flow velocities. Moreover, almost the same patterns are found as in the base case.

4.3 Quantification of spatial variability

4.3.1 Quantification method

To provide insight in the magnitude of influence by sand wave fields on wind waves when changing its configuration, a quantification method is introduced. The spatial variability for a certain area is quantified by finding the maximum value, mean value, minimum value and standard deviation inside this area. It is chosen to look at the change of wind wave behaviour above the crest and troughs of the sand waves and above the full area of interest (see Figure 4.1).

In order to determine the area of the sand wave crests and troughs, respectively the highest and lowest 10% of the bed elevation are isolated. Subsequently, the output inside these areas is being quantified.

To assess the influence of parameters, the base case which was already introduced in the previous section, is also considered here. In the following subsections, one parameter is changed and the influence on the Amplification Factors and near-bed orbital velocities is assessed. Because of the numerous amount of graphs, they are all given in Appendix C. In these graphs the following information is shown:

- the *upward pointing triangle* shows the maximum found value inside this area;
- the *downward pointing triangle* shows the minimum found value inside this area;
- the *red circle* shows the average value inside this area;
- the *gray area* shows the band of one time the standard deviation from the mean. Therefore it gives an impression of the variability.

Finally, in the last subsection, the influence of all parameters are summarized in a sensitivity analysis to show the mutual influence of the parameters.

4.3.2 Sand wave orientation

Figure C.1a, C.1c and C.1e show the amplification of the wind wave amplitude due to change of sand wave orientation, respectively above the sand wave crests, troughs and whole area of interest. Above the sand wave crests, it can be seen that the amplitudes of the wind waves start to amplify for orientation angles greater than about 55 degrees, indicating shoaling. Smaller orientations barely show amplification of the wind wave amplitude. Between orientation angles of 65 and 80 degrees, the mean amplification of wind wave amplitude decreases above the sand wave crests, and increases above the sand wave troughs. Also, between the latter orientations, increase of wind wave amplitude is found above the troughs. For orientation angles larger than 80 degrees, the

mean amplification of wind wave amplitude above the crests and troughs significantly increase and decrease, respectively. Furthermore, the standard deviation increases when the orientation angle approaches perpendicularity with respect to the incident wind wave crest. Above the whole area of interest, the maximum found wind wave amplitude and standard deviation increase whereas the mean wind wave amplitude decreases slightly for an increasing orientation angle.

Figure C.1b, C.1d and C.1f show the amplification of the near-bed flow velocity due to change of sand wave orientation, respectively above the sand wave crests, troughs and whole area of interest. Roughly similar behaviour is visible as that of the amplification of wind wave amplitude. Further, for orientations below 55 degrees, the near-bed velocities slightly increase above the sand wave crests and slightly decrease above the sand wave troughs with respect to near-bed velocity above the flat-bed. Above the whole area of interest, the maximum found near-bed velocity and standard deviation increase when the orientation angle reaches perpendicularity with respect to the incident wind wave crest.

4.3.3 Mean water depth

Figure C.2a, C.2c and C.2e show the amplification of the wind wave amplitude due to change of the mean water depth, respectively above the sand wave crests, troughs and whole area of interest. Above the sand wave crests, the maximum, minimum and standard deviation of wind wave amplitude decrease when it becomes deeper. Above the troughs, the wind wave amplitudes do not become higher. Also, above the troughs a local maxima and minima are visible. Visual inspection showed that the zones of minimum found amplification shift towards to slopes of the sand waves and are therefore not found above the troughs, nor the crests. This is confirmed when looking at the whole area of interest, which shows that the minimum found amplifications are mostly located above the slopes of sand waves.

Figure C.2b, C.2d and C.2f show the amplification of the near-bed flow velocity due to change of the mean water depth, respectively above the sand wave crests, troughs and whole area of interest. Roughly, similar behaviour is visible as that of the amplification of wind wave amplitude. In case of shallow water, the near-bed velocity can, in our configuration, become three times as strong above the sand wave crests as above the flat-bed.

4.3.4 Sand wave length

Figure C.3a, C.3c and C.3e show the amplification of the wind wave amplitude due to change of the sand wave length, respectively above the sand wave crests, troughs and whole area of interest. Above the sand wave crests, the maximum and mean amplification of wind wave amplitude, as well as the standard deviation increase when sand wave length increases, indicating stronger shoaling. Furthermore, above the crests and troughs local

maxima and minima are found. Due to slower or faster refraction processes, the zones of amplification shift in the x coordinate. Hence, due to the restriction a calculation domain (i.e. area of interest) certain information can be positioned outside this domain and therefore local maxima and minima are found in the graphs. The whole area of interest shows that for sand wave lengths bigger than 300 meter, locations are found where the wind wave amplitude is zero, indicating destructive interference.

Figure C.3b, C.3d and C.3f show the amplification of the near-bed flow velocity due to change of the sand wave length, respectively above the sand wave crests, troughs and whole area of interest. Roughly, similar behaviour is visible as that of the amplification of wind wave amplitude. Near-bed velocities increase above the crest when the sand waves become longer, upto three times as strong as the near-bed velocity at the flat-bed.

4.3.5 Sand wave height

Figure C.4a, C.4c and C.4e show the amplification of the wind wave amplitude due to change of the sand wave height, respectively above the sand wave crests, troughs and whole area of interest. Above the sand wave crests, it can be seen that the maximum found amplification and standard deviation increase with sand wave height. Also, for sand wave heights between approximately 1 and 2.5 meter it is visible that the minimum found amplification factor above the sand wave crests is higher than 1. The latter means that apparently anywhere above the sand wave crests wind waves are increased in amplitude. Above the troughs, a drop in mean and minimum amplification of the wind amplitude is found around a height of 1.8 meter. When looking at the whole area of interest, it can be concluded that location where the wind wave amplitude is zero are mostly located above the slopes of the sand waves.

Figure C.4b, C.4d and C.4f show the amplification of the near-bed flow velocity due to change of the sand wave height, respectively above the sand wave crests, troughs and whole area of interest. Roughly, similar behaviour is visible as that of the amplification of wind wave amplitude. The maximum and mean near-bed velocities and standard deviation increase above the sand wave crests when sand wave height increases. Above the troughs, near-bed velocities decrease.

4.3.6 Sand wave asymmetry

Figure C.5a, C.5c and C.5e show the amplification of the wind wave amplitude due to change of the asymmetry factor, respectively above the sand wave crests, troughs and whole area of interest. Above the sand wave crests, the maximum found amplification of wind wave amplitude slightly decreases and the standard deviation decreases when sand waves become more asymmetric. Above the troughs, the mean amplification of wind wave amplitude slightly drops, whereas the maximum found amplification and standard deviation increase when sand waves become more asymmetric. Lastly, above the whole area of interest, no significant change is visible.

Figure C.5b, C.5d and C.5f show the amplification of the near-bed flow velocity due to change of the asymmetry factor, respectively above the sand wave crests, troughs and whole area of interest. Roughly, similar behaviour is visible as that of the amplification of wind wave amplitude.

4.3.7 Wave period

Figure C.6a, C.6c and C.6e show the amplification of the wind wave amplitude due to change of the wind wave period, respectively above the sand wave crests, troughs and whole area of interest. Wind wave periods bigger than $T = 6$ seconds are assessed due to the earlier mentioned RAM restriction (see Section 2.5). Above the sand wave crests, the amplifications of the wind wave amplitudes are relatively constant, only at short periods, the mean amplification shows slightly higher magnitudes. Also at these smaller periods, the standard deviation is less above the sand wave crests. Although differences are small, above the troughs the mean amplification factor shows a maximum around 8 to 9 seconds. Also the standard deviation above the troughs is smaller for short wind wave periods. When looking at the full area of interest, relatively constant behaviour can be seen for the mean, maximum and standard deviation of amplification factors.

Figure C.6b, C.6d and C.6f show the amplification of the near-bed flow velocity due to change of the wind wave period, respectively above the sand wave crests, troughs and whole area of interest. Roughly, similar behaviour is visible as that of the amplification of wind wave amplitude. The highest amplification of near-bed flow velocities are found above the sand wave crests and in case of shorter wind wave periods. The amplification of mean near-bed velocity drops above the sand wave crests when the wind wave period becomes longer. Above the troughs, the standard deviation increases when the wind wave period becomes longer. Furthermore, when comparing the latter with the distribution above the whole area of interest, it can be concluded that the lowest near-bed velocities are found above the slopes of sand waves.

4.3.8 Parameter sensitivity analysis

To assess the mutual influence of the parameters on amplification of the wind wave amplitude and near-bed orbital velocities, the influences of the parameters in the previous section are summarized in a comprehensive sensitivity analysis. The parameter configuration as used in the base case is considered as the starting point, which is located at the points where all lines intersect as can be seen in Figure 4.9 and 4.10. To combine all the parameters on the x axis, a percentage scale is used (e.g. $\lambda_b = 500$ [m] in the base case, equals 100% on this scale and $\lambda_b = 250$ [m] equals 50% on this scale). The indicator used to quantify the sensitivity is the maximum found amplification, factor $\mathrm{AF}_{\mathrm{A,aoi,max}}$, and maximum amplification of near-bed flow velocity $\mathrm{AF}_{\mathrm{nb,aoi,max}}$, inside the full area of interest, as it is believed that these indicators give the best representation of the influence of a sand wave field on wind waves.

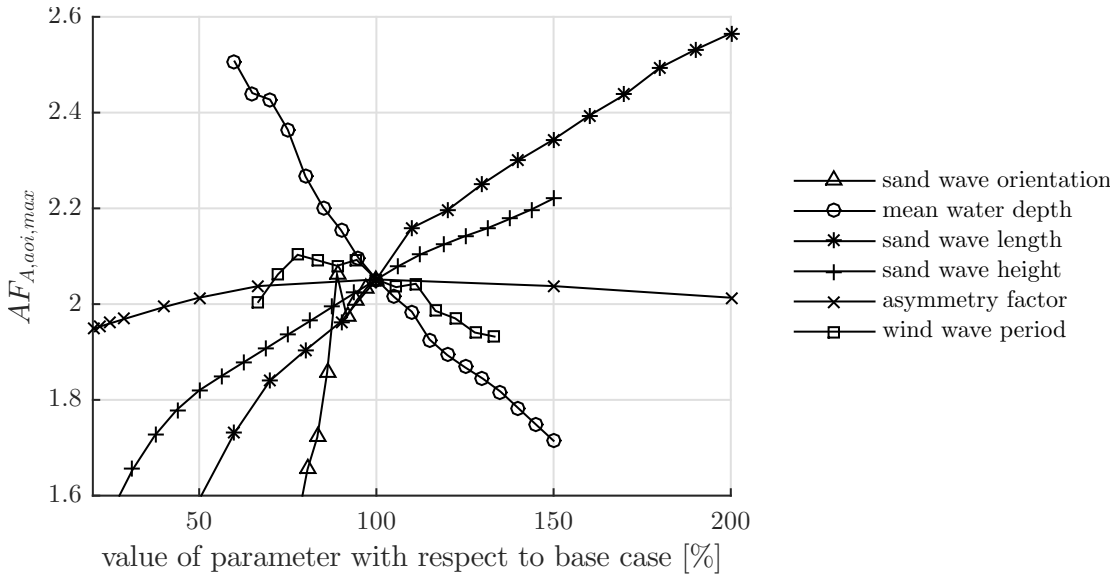

Figure 4.9: Parameter sensitivity analysis of the base case on the influence of the maximum found amplification of the wind wave amplitude (AF_A) above the full area of interest.

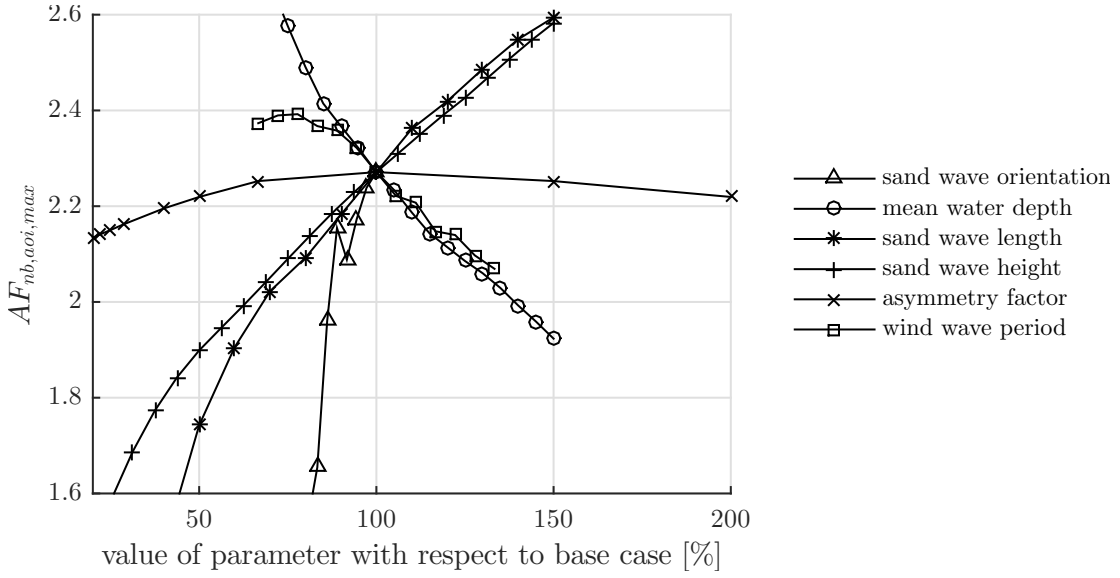

Figure 4.10: Parameter sensitivity analysis of the base case on the influence of the maximum found amplification of the near-bed flow velocity (AF_{nb}) above the full area of interest.

Figure 4.9 depicts the sensitivity of parameters on the maximum amplification of the wind wave amplitude found in the area of interest. Sand wave orientation, sand wave length, sand wave height and the mean water depth show significant influence. The wind wave period and asymmetry factor have less influence.

Figure 4.10 depicts the sensitivity of parameters on the maximum amplification of

near-bed orbital flow velocity in the area of interest. The influence of sand wave orientation is strong. Furthermore, the mean water depth, sand wave length, sand wave height and wind wave period have relatively strong influence whereas the influence of the asymmetry factor is small.

4.4 Bragg Resonance

Bragg Resonance (see Section 1.1.3) is caused by reflection of wave components due to a wavy bathymetry resulting in constructive interference (i.e. superposition). For the model-specific situation this Bragg Resonance occurs when the following condition is satisfied:

$$n\lambda = 2\lambda_b \cos(\theta_b), \tag{4.4}$$

where n indicates a multiple of the wind wave length λ, and λ_b is the sand wave length. Due to the dispersion relationship, the wavelength of the wind wave varies when travelling over a sand wave, hence strictly there is no constant wind wave length λ. In this section, an assessment is performed to find conditions where constructive interference due to Bragg Conditions (i.e. Bragg resonance) might become evident.

In Figure 4.11 the maximum found amplification factor of the wind wave amplitude above the full area of interest $AF_{A,aoi,max}$ is explored for varying combinations of sand wave length and orientation of the sand wave field. Assuming a constant wave length as found above the flat-bed configuration, the red dash dotted lines are locations where, according to the theory, Bragg's Law (Eq. (4.4)) is satisfied. In this figure it is visible that the highest amplifications of wind wave amplitude are found in case of long sand wave lengths and orientations of the sand wave crests perpendicular to the wind wave crests. However, maybe even more interesting is the visible curved zone of amplification

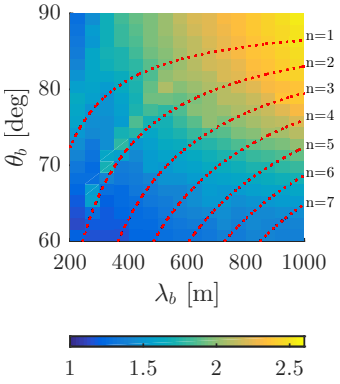

Figure 4.11: Exploring possible Bragg Resonance for combinations of λ_b and θ_b: base case

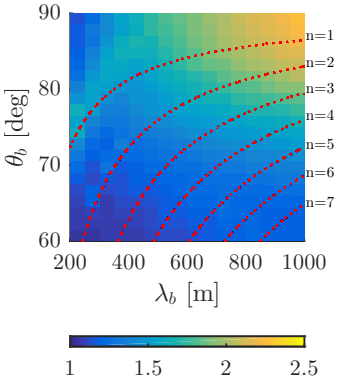

Figure 4.12: Exploring possible Bragg Resonance for combinations of λ_b and θ_b: Base Case with $H_b = 2$ meter.

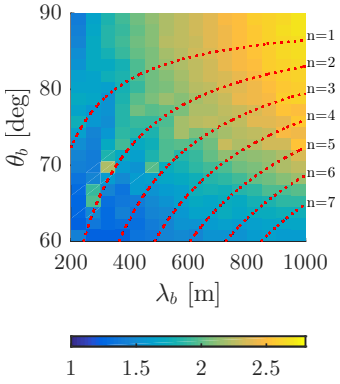

Figure 4.13: Exploring possible Bragg Resonance for combinations of λ_b and θ_b: Base Case with $H_b = 6$ meter.

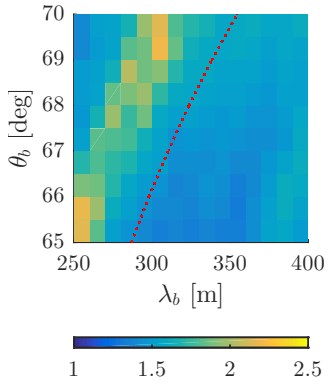

Figure 4.14: Exploring possible Bragg Resonance for combinations of λ_b and θ_b: Base Case with $H_b = 6$ meter: zoomed.

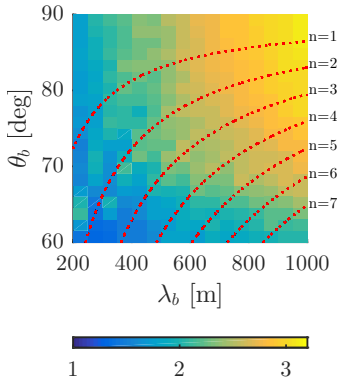

Figure 4.15: Exploring possible Bragg Resonance for combinations of λ_b and θ_b: Base Case with $\bar{h} = 12$ meter.

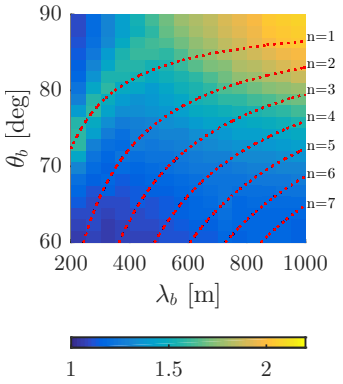

Figure 4.16: Exploring possible Bragg Resonance for combinations of λ_b and θ_b: Base Case with $\bar{h} = 30$ meter.

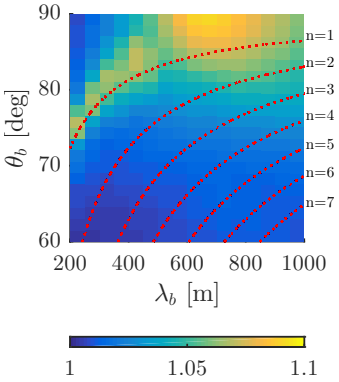

Figure 4.17: Exploring possible Bragg Resonance for combinations of λ_b and θ_b: Base Case with $H_b = 0.1$ meter.

found in the domain of $200 \leq \lambda_b < 600$ and $60 \leq \theta_b \leq 83$, indicating local maxima. Although, this curved zone of amplification is not positioned exactly above the Bragg Condition lines (i.e. red dash dotted line where $n = 2$), it shows similarities.

In Figure 4.12 the base case (Figure 4.11) is adjusted to a lower sand wave height of $H_b = 2$ meter. Now, the curved zone of amplification from Figure 4.11 has almost vanished. However, at the $n = 1$ Bragg Condition line a curved zone of amplification exists, which is possibly related to Bragg Resonance. Furthermore, the influence at long sand wave lengths and perpendicular orientated sand wave crests decreased.

In Figure 4.13a the base case (Figure 4.11) is adjusted to a higher sand wave height of $H_b = 6$ meter. Now it seems that multiple curved zones of amplification (i.e. at $n = 2$

and $n = 3$) are present. Apparently when sand wave height increases, Bragg Resonance becomes more evident. The latter can possibly be explained that wave components are easier reflected when the slopes of the sand wave are steeper. When zooming in on a part of this curved zone of amplification as depicted in Figure 4.14, a clear stroke of amplification is found slightly off-positioned with respect to the Bragg Condition line.

In Figure 4.15 the base case (Figure 4.11) is adjusted to a smaller water depth of $\bar{h} = 12$ meter. It seems that even more curved zones of amplification are present now. Furthermore, due to the smaller water depth the influence of the sand wave field in general is higher.

In Figure 4.16 the base case (Figure 4.11) is adjusted to a larger water depth of $\bar{h} = 30$ meter. The overall darker colors compared to the base case indicate that the overall influence of the sand wave field is less. Furthermore, a single, relatively wide curved zone of amplification is visible at the $n = 1$ Bragg Condition line.

Lastly, in Figure 4.17 the base case (Figure 4.11) is adjusted to a very small sand wave length $H_b = 0.1$ meter. In this situation we expect that non-linear effects are not yet significantly present. Also please note that the colorbar is adjusted to a smaller range. Although the amplifications are minor, a clear curved zone of amplification is visible at the $n = 1$ Bragg Condition line. Furthermore, in contradiction to the other cases the highest amplifications in the area of interest are no longer found at the largest sand wave lengths, but show a maximum at about 600 to 700 meter and an orientation of 90° degrees.

4.5 Observed sand wave fields in the North Sea

In this section the wind wave propagation over observed sand wave fields in the North Sea are assessed. The raw, observed bathymetric data needs to be manipulated such that it can be put in the model. Therefore first the observed data was interpolated such that it fit in the 5000 by 5000 meter domain with a space step of 5 meter. Secondly, after subtracting the mean observed water depth, a tapering function was used to create the patch-like structure of the sand wave field with a flat-bed surrounding it. A circular tapering function (see Appendix A.5) was used such that the observed sand wave field could be rotated easily within the domain[1]. In Figure 4.18 the area of interest and the dimensions of the circular tapering function are visualized.

Four observed sand wave fields are used to assess wind wave behaviour above them. Figure 4.19, 4.20, 4.21 and 4.22 show, in sequence, a relatively irregular sand wave field with lots of bifurcations and short sand wave lengths to a more regular sand wave field pattern with longer sand wave lengths. In these figures, part of the sand wave crests are visualized by black lines for easier reference.

In Figure 4.19b and Figure 4.19c the amplification of wind wave amplitude above a relatively irregular sand wave field is visualized. Reflections caused by the boundaries of the model are visible and hence interpretation of the results should be done carefully.

[1] the `imrotate()` function of MATLAB was used

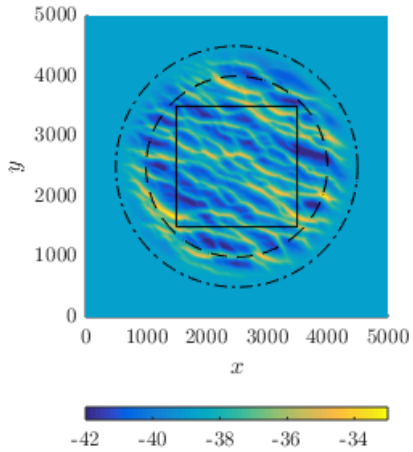

Figure 4.18: Definition of the area of interest and circular tapering function. The dash-dotted line where the transition starts from the flat-bed configuration to the sand wave field, the dashed line is where the sand wave field is fully developed and the solid line represents the area of interest.

Zones of amplification of the wind wave amplitude are visible, but are not directly related to the patterns of the local water depth in Figure 4.19a and 4.20a, respectively. However, in Figure 4.19c and Figure 4.20c, the amplification of near-bed orbital flow velocity is depicted and shows roughly similar patterns to the bed elevation. Hence, the near-bed velocities caused by these bathymetries, which are also relatively deep and the sand waves slopes are relatively steep, are mainly caused by change of local water depth and not so much by the shoaling effect of wind waves. Further, it is visible that the near-bed flow velocity is amplified stronger than the wind wave amplitude in both figures.

In Figure 4.21b and Figure 4.22b, the amplification of wind wave amplitude for two more regular observed sand wave fields is visualized. Also these two sand wave fields are positioned in a relatively smaller mean water depth compared to the sand wave fields in 4.19 and Figure 4.20. In Figure 4.21, zones of amplification of the wind wave amplitude are clearly visible that are slightly deviated from the orientation of the sand wave crests. Apparently, due to refraction, the wind waves do not necessarily show shoaling above the sand wave crests but also above the troughs of sand waves. in Figure 4.22b, the zones of amplification are less apparent, possibly because the sand waves are not so high. Furthermore, in 4.21c and Figure 4.22c the amplification of the near-bed flow velocity is visualized. The near-bed flow velocity now shows similar patterns to that of the amplification of the wind wave amplitude. Hence, the process of shoaling is now more controlling the near-bed flow velocity than the change in local water depth due to bed elevation.

The interference patterns that are visible in Figure 4.19 to 4.22 might, possibly, cause irregularities in the sand wave field and be a possible explanation of for example bifurcations.

Furthermore, a closer look is given when the observed sand wave field in Figure 4.21 is oriented differently with respect to the incident wind wave. In Figure 4.23 the latter is visualized, with symbols as explained in Section 4.3.1. The orientation is anticlockwise with respect to its current position as shown in Figure 4.21. At a rotation of approximately 50 degrees, the sand wave crests are more or less oriented parallel to the sand wave crests, and shows that spatial variability of the wind waves decreases. In contradiction, at a rotation of approximately -30 degrees, the sand wave crests are approximately orientated perpendicular to the incident wind wave crests and show great spatial variability.

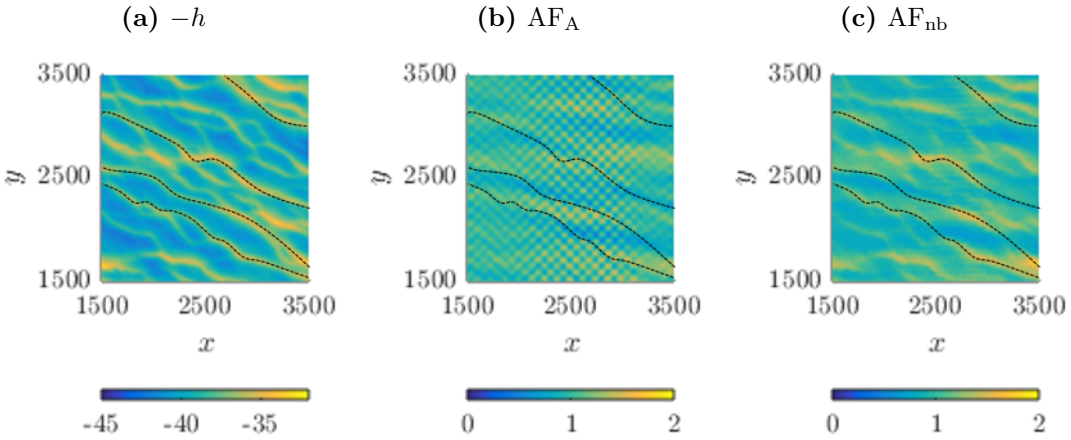

Figure 4.19: Visualization of the spatial variability caused by a observed sand wave field in the Southern Bight of the North Sea (coordinates: UTM 31U 470000 5740000). (a) shows the local water depth, (b) the amplification of the wind wave amplitude, (c) the amplification of the near-bed flow velocity.

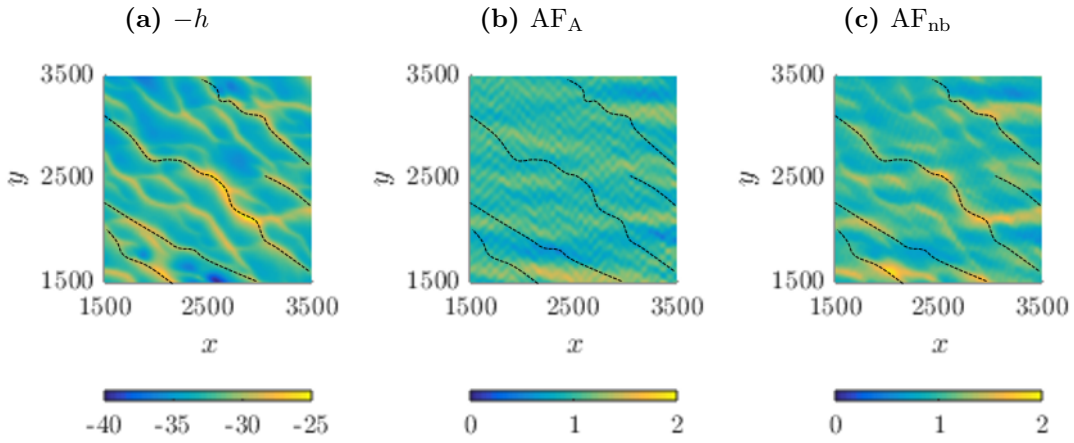

Figure 4.20: Visualization of the spatial variability caused by an observed sand wave field in the Southern Bight of the North Sea (coordinates: UTM 31U 510000 5760000). (a) shows the local water depth, (b) the amplification of the wind wave amplitude, (c) the amplification of the near-bed flow velocity.

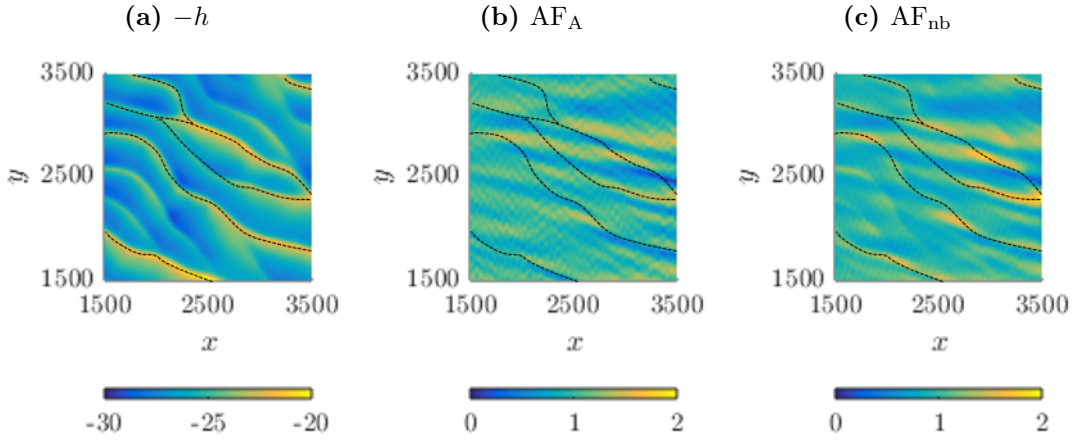

Figure 4.21: Visualization of the spatial variability caused by an observed sand wave field in the Southern Bight of the North Sea (coordinates: UTM 31U 550000 5781000). (a) shows the local water depth, (b) the amplification of the wind wave amplitude, (c) the amplification of the near-bed flow velocity.

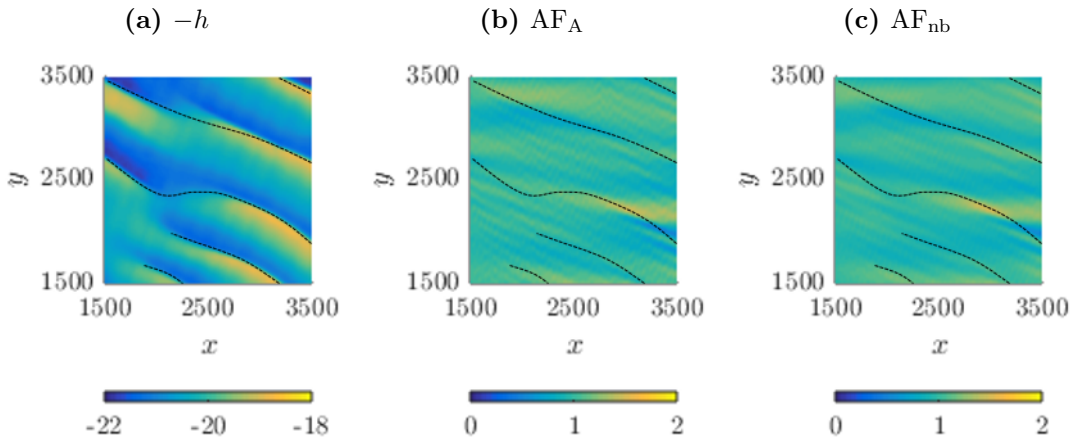

Figure 4.22: Visualization of the spatial variability caused by an observed sand wave field in the Southern Bight of the North Sea (coordinates: UTM 31U 575000 5792000). (a) shows the local water depth, (b) the amplification of the wind wave amplitude, (c) the amplification of the near-bed flow velocity.

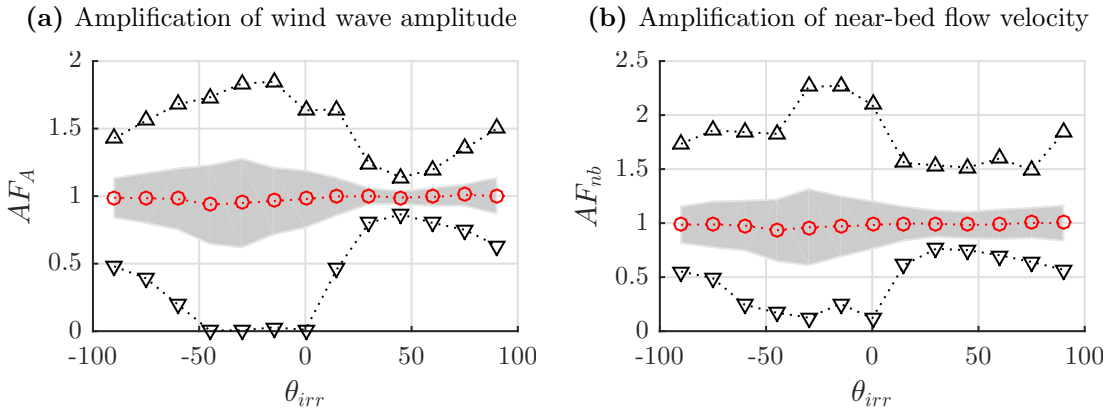

Figure 4.23: Spatial distribution for different orientations of the observed sand wave field as given in Figure 4.21. Orientation is measured anticlockwise from the situation as given in Figure 4.21. The symbols denote: △ max, ▽ min, ◯ mean and the gray area shows the standard deviation.

Chapter 5

Discussion

5.1 Model

Modelling the true behaviour of wind-generated surface gravity waves (i.e. wind waves) is rather difficult due to the combined effects of several physical processes. In order to mathematically express the behaviour of wind waves, assumptions and simplifications are made to formulate the latter. The Mild-Slope Equation, which is the governing model equation, assumes linear harmonic waves, an inviscid, incompressible fluid, irrotational flow but moreover a slight variation of water depth over the distance of a wind wave length, i.e. a mild-sloping bathymetry. Beside these assumptions, boundary conditions are imposed in the model which require a priori knowledge about the angle of the incidence of the wind wave on these boundaries. In this model, these angles are estimated to be the same as the angle of the predefined incident, monochromatic wind wave at the incoming boundary. Errors in the expression of these boundary conditions might be reduced by for example iterative updating of these boundary conditions. All in all, the model is able to output the complex valued amplitudes, which should be interpret carefully due to the aforementioned assumptions.

Furthermore, the large system matrix that has to be stored to use the direct-solution method limits the number of nodes. An iterative solution method will eliminate this limitation at the cost of possibly slower calculation speeds and convergence criterions.

Lastly, the model is verified with an analytical solution under the assumption of a flat-bed configuration. This verification method is considered normative for the accuracy of the model. An analytical solution in case of bathymetric configuration including a sand wave field might be more representative as a method for verification, however the analytical solution to this situation is more difficult, if it exists.

5.2 Bathymetry generation

The model is able to generate a regular bathymetric profile of a sand wave field based on input parameters: sand wave height, sand wave length, asymmetry and orientation of the sand wave crests. Irregularities as for example variable spacing between sand waves

or local increase in sand wave heights can not be produced. However, field-data (i.e. observed water depths) or manually adjusted water depths can be used as input.

Furthermore, to gently introduce the sand wave field, a tapering function is used. This tapering function describes a linear transition from the flat-bed configuration to the sand wave field and therefore has a trapezium shape. A sinusoidal shaped transition between the flat-bed and sand wave field will describe the transition even more gently. The tapering function will then look like a *Tukey* window. A quick comparison of the Tukey window with the current used tapering window at the regular sand wave field patterns, showed maximum differences of 5% inside the area of interest. Another option for the tapering window can be a circular window (see Appendix A.5) as used for the observed sand wave fields. The latter makes rotation of an observed data set easier, however more information is lost.

5.3 Assessment of results

This MSc project is conducted to assess the influence of sand wave fields on wind waves. The influence on wind waves is made insightful and quantifiable by assessing the spatial variability of amplification factors of the wind wave amplitude and the corresponding near-bed orbital flow velocities inside the domain. Subsequently, a base configuration with certain parameter settings is established. From there a parameter is changed individually and the change of spatial variability due to this change in parameter is assessed. The base case is chosen based on a high influence situation, which is when the sand wave crests were orientated perpendicular to the wind wave crests. This orientation however causes a symmetric situation and might therefore be a somewhat risky base case. Also, the results may describe very case specific behaviour and therefore the generality of the results may be questioned. To come to more generic conclusions, combinations of parameters should be assessed for their influence on wind waves and this method of assessment might therefore not be that suitable. From the results in this thesis, it became for example evident that the orientation angle has a significant influence on the effect of other input parameters (e.g. sand wave height and sand wave length), such that research to the influence of changing combinations of these parameters may result in more in-depth knowledge about the relations of parameters to the effect size. in Section 4.4 however, the influence of various combinations of orientation angles and sand wave lengths were explored, which resulted in local maxima of influence (likely Bragg Resonant cases). As this shows that local maxima exist, it may be required to enhance full exploration of the influence on wind waves by all combinations of parameters: simply assuming linear or exponential behaviour between two parameter values is therefore not sufficient. To prevent extremely numerous of combinations and with that very high computational cost, the parameter space can be reduced from currently 7 to 4 parameters by a scaling procedure of the Mild-Slope Equation to its dimensionless form. The formulation of this dimensionless Mild-Slope Equation is introduced in Appendix D.

Furthermore, in order to quantify spatial variability of the amplification factors and near-bed orbital flow velocity, the maximum, minimum, mean and standard deviation

are determined for areas above the sand wave crests, sand wave troughs and the full area of interest. This choice is made as it is believed that this gives an adequate quantification of the spatial variability. However, one might find other quantification methods more suitable (e.g. whisker plots). Also, for some analysis (i.e. sensitivity analysis and Bragg Resonant situations) it was required to accommodate the spatial variability of the full area of interest in one indicator. The maximum found amplification factor of the wind wave amplitude above the full area of interest was chosen for this single indicator. The latter is done as it is believed that the maximum influence is herewith expressed, however one may be more interested in other single indicators as for example the mean value or the standard deviation).

The result showed that the zones of amplification of wind wave amplitude and near-bed orbital velocity can move outside the area of interest because of stronger or weaker refraction processes. Therefore, essential information can be positioned outside our calculation domain and hence is not incorporated in our analysis. Further, the influence of an observed, irregular sand wave field caused noisy reflections due to the boundary conditions, hence interpretation should be done carefully.

The results showed that sand wave fields are able to amplify wind wave amplitude and causes spatial variability in wind wave propagation. Subsequently, this increasing or decreasing wind wave amplitude has effect on the strength of the near-bed orbital velocity and consequently on morphodynamic processes. The SMARTSEA project is investigating the influence of wind waves on sand waves, hence this knowledge on spatial variability in near-bed orbital flow velocities induced by the shoaling, refraction and reflection effects of the incidental wind waves can change sand wave dynamics and will likely cause spatial variability among a sand wave field.

Lastly, it is relatively hard to find observed data of surface elevation such as satellite imagery to validate the model outcomes with. The first reason is that the model assumes perfect monochromatic wind waves which are incident only from one direction. When speaking of a domain size of kilometres, it is almost impossible to find such conditions. Secondly, the way to retrieve such data is a very costly business and might therefore not be in reach from a financial perspective. However, when bathymetric data and a satellite image of the surface elevation at this specific location are available, the model output may possibly be validated qualitatively. Furthermore, it might be possible to recreate the situation in a laboratory. As far as we know, no experiments have been carried out to the behaviour of wind waves above a wide extending sand wave field in both horizontal directions. Subsequently, the measured data from this experiment could then possibly be used for validation. Finding situations which create the possibility to validate the model as formulated in this thesis may be a topic for future research.

Chapter 6

Conclusion and Recommendations

6.1 Conclusion

The aim of this thesis was to investigate the influence of sand wave fields in a shallow sea on incident wind waves. Therefore, first a hydrodynamic model based on the Mild-Slope Equation was formulated which is able to model wind wave behaviour when propagating over a wavy bathymetry. The model has a square domain with the West boundary describing the incident wind wave with a Dirichlet type boundary condition. The other boundaries physically represent open sea, and are described with non-reflective boundary condition based on the Sommerfeld Radiation Condition. For our system the latter resulted in Neumann type boundary conditions at the North and South boundary and a boundary condition of Robins' type on the East boundary. In order to minimize interference with the boundaries, the boundary conditions are formulated a far distance from the sand wave field. The latter is implemented by locating a sand wave field patch in the middle of the domain surrounded by a flat-bed configuration.

The model equation was then approximated by finite differences. Subsequently, the resulting system of linear equations was solved by a direct solution method. The numerical implementation of the model was done in MATLAB.

Lastly, the model was verified with an analytical solution in case of a flat-bed configuration. Restrictions of the capacity of the computer used to run the simulations showed that the accuracy of the model needed to be set to a Root-Mean Square Error (RMSE) of 1%. The latter was necessary to solve a numerical system of $5,000$ by $5,000$ meter with a space step of $\Delta x = \Delta y = 5$ meter.

Subsequently, a bathymetric dataset is required as input for the model. The regular sand wave fields are formulated by means of a bed elevation function consisting of a plane wave with a specific orientation, sand wave height and sand wave length. Asymmetry is included by merging together two different sinusoidal wave signals at the same phase but characterized by different wave lengths. Lastly, to generate the patch-like sand

wave field surrounded by a flat-bed configuration as explained at the previous research question, a tapering function is formulated. This tapering function describes a two-dimensional trapezium shaped structure with values ranging between 0 and 1 which is multiplied with the bed elevation data. The observed bathymetric dataset was manipulated with a circular tapering function such that the dataset could be rotated more easily.

Due to the influence of sand wave fields, wind waves will show spatial variability caused by refraction, shoaling and reflection. The spatial variability of the wind wave is assessed by looking to the amplification of the pre-defined amplitude of the incident wind wave and the near-bed orbital flow velocity beneath the wind waves. The latter can be visualized by using a top-view colormap where low values are indicated with a dark, blue color and high values are indicated with a bright, yellow color. Furthermore, an area of interest is established which is smaller than the area of the sand wave field patch. The latter is done to prevent visualization and quantification of distortion caused by the transition of the flat-bed to the sand wave field patch. Subsequently, the spatial variability was quantified by looking at the distribution of the data above the sand wave crests, -troughs and full area of interest. This was done by determining the maximum and minimum found value and the mean and standard deviation inside these areas.

From the results can be concluded that the orientation of the sand wave field has a major influence on the influence of the other parameters. Therefore the orientation of the sand wave field with respect to the incident wind wave is very dominant compared to other parameters.

When looking at the amplification of the wind wave amplitude and near-bed orbital flow velocity, water depth, sand wave length and sand wave height show significant influence. Wind wave period and asymmetry show less influence. Specific combinations of parameters even show local maxima of influence which might be associated by Bragg Resonance. A maximum amplification of approximately three times the wind wave amplitude was found in case of a small water depth, long sand wave length, high sand wave crests and sand wave crests orientated perpendicular to the crests of the incident wind waves. In the latter case, also the highest near-bed orbital flow velocities were found at the crests of the sand waves, upto three times as high as the near-bed flow velocity in case of a flat-bed.

Lastly, in case of observed sand wave fields, the boundary conditions of the model showed noisy reflections. Furthermore, the zones of amplification of the wind wave amplitude were the strongest for the relatively shallower locations and were overall slightly deviated from the orientation of the sand wave crests. At the shallower locations, the amplification of the near-bed flow velocity is more dominated by wind wave amplitude whereas at deeper locations the changing local water depth caused by the sand wave field is more dominant. The visible interference patterns of near-bed velocity were not always in union with the change of bed elevation. Also, possibly this might be an explanation for spatial variability of bed elevation among the sand wave field.

6.2 Recommendations

For further work in this field it is recommended to analyse the influence of simultaneous change of parameters. The current assessment method, by means of a base configuration and individually changing parameters from there, might not be sufficient to gain in-depth knowledge about the influence of sand wave fields. The reduction of the parameter space due to formulation of the model equation in a dimensionless form as introduced in Appendix D is also recommended to use. The latter will prevent using parameter configurations which is essence describe similar conditions.

Furthermore, it is recommended to find methods for validation of the model output. The current output may theoretically be correct but it is currently unknown if the findings correspond with real observations. An experiment in a laboratory where a sand wave field patch is recreated in both horizontal coordinates might give the required data and insights to validate the model outcomes.

For the SMARTSEA project it is recommended to incorporate spatial variability in near-bed orbital velocities induced by shoaling, refraction and reflection of the wind waves. The locally changing near-bed velocities are not always in union with the bed elevation and hence will affect sand wave dynamics by locally stronger or weaker morphodynamics then expected.

References

S. Aliotta and G. Perillo. A Sand Wave Field in the Entrance to Bahia Blanca Estuary, Argentina. *Instituto Argentino de Oceanografia*, pages 1–14, 1986.

P. Barnard, D. Hanes, and R. Kvitek. Giant sand waves at the mouth of San Fransisco Bay. *EOS*, 97:285–289, 2006.

J.C.W. Berkhoff. Computation of combined Refraction-Diffraction. Technical report, Delft Hydraulic Laboratory, Delft, 1972.

J.C.W. Berkhoff. *Mathematical Models for Simple Harmonic Linear Water Waves: Wave Diffraction and Refraction*. PhD thesis, Technical University of Delft, 1976.

G. Besio, P. Blondeaux, M. Brocchini, and G. Vittori. On the modelling of sand wave migration. *Journal of Geophysical Research*, 109(C04018), 2004.

G. Besio, P. Bondeaux, M. Brocchini, S.J.M.H. Hulscher, D. Idier, M.A.F. Knaapen, A.A. Németh, P.C. Roos, and G. Vittori. The morphodynamics of tidal sand waves: A model overview. *Coastal Engineering*, (55):657–670, 2008.

R. Bijker, J. Wilkens, and S.J.M.H. Hulscher. Sandwaves: where and why. *Proceedings of the Eighth (1998) International Offshore and Polar Engineering Conference*, 2, 1998.

N. Booij. A Note on the Accuracy of the Mild-Slope Equation. *Coastal Engineering 7*, 7:191–203, 1983.

Y. Catano-Lopera and M. Garcia. Geometry and migration characteristics of bed forms under waves and currents Part 2: Ripples superimposed on sand waves. *Coastal Engineering*, 53:781–792, 2006.

R.A. Dalrymple, K. Duck Suh, J. Kirby, and J. Won Chae. Models for wide-angle water waves and wave diffraction, part 2: Irregular bathymetry. *Journal of Fluid Mechanics*, 201:299–322, 1989.

A.G. Davies and A.D. Heathershaw. Surface wave propagation over sinusoidally varying topography: theory and observation. *Institute of Oceanographic Sciences*, 159(181), 1983.

R.G. Dean and R.A. Dalrymple. Water Wave Mechanics for Engineers & Scientists. *Advanced Series Ocean Engineering*, 2, 1991.

T. Van Dijk and M. Kleinhans. Processes controlling the dynamics of compound sand waves in the North Sea. *Journal of Geophysical Research*, 110:1–15, 2005.

M. Dingemans. *Water wave propagation over uneven bottoms.* PhD thesis, Technical University Delft, Delft, 1994.

N. Dodd, P. Blondeaux, D. Calvete, H.E. de Swart, A. Falqués, S.J.M.H. Hulscher, G. Rózynski, and G. Vittori. Understanding Coastal Morphodynamics Using Stability Methods. *Journal of Coastal Research*, 19(4):849–865, 2003.

L. Dorst, P.C. Roos, and S.J.M.H. Hulscher. Spatial differences in sand wave dynamics between the Amsterdam and the Rotterdam region in the Southern North Sea. *Continental Shelf Research*, 31:1096–1105, 2011.

D. Givoli. Non-reflecting Boundary Conditions. *Journal of Computational Physics*, 94: 1–29, 1991.

P. Harris. Sandwave movement under tidal and wind-driven currents in a shallow marine environment: Adolphus Channel, northeastern Australia. *Continental Shelf Research*, 9(11):981–1002, 1989.

S.J.M.H. Hulscher. Tidal-induced large-scale regular bed form patterns in a three-dimensional shallow water model. *Journal of Geophysical Research*, 101:727–744, 1996.

S.J.M.H. Hulscher and G.M. van den Brink. Comparison between predicted and Observed Sand Waves and Sand Banks in the North Sea. *Journal of Geophysical Research*, 106(C5):9327–9338, 2001.

S.J.M.H. Hulscher, H. de Swart, and H.J. de Vriend. The generation of offshore tidal sand banks and sand waves. *Continental Shelf Research*, 13(11):1183–1204, 1993.

M.A.F. Knaapen. Sandwave migration predictor based on shape information. *Journal of Geophysical Research*, 110(F04S11):1–9, 2005.

D. Langhorne. A Sandwave Field in the outher Thames estuary, Great Britain. *Marine Geology*, 14:129–143, 1973.

Y. Liu and D. Yue. on Generalized Bragg scattering of Surface Waves by Bottom Ripples. *Journal of Fluid Mechanics*, 356:297–326, 1998.

M. Longuet-Higgins and R. Stewart. Radiation stresses in water waves: a physical discussion. *Deep-Sea Research*, 11:529–562, 1964.

I. McCave. Sand waves in the North Sea off the coast of Holland. *Marine Geology*, 10: 199–225, 1971.

A. Németh, S.J.M.H. Hulscher, and H.J. de Vriend. Modelling sand wave migration in shallow shelf seas. *Continental Shelf Research*, 27:2795–2806, 2002.

A.A. Németh, S.J.M.H. Hulscher, and R.M.J. Van Damme. Simulating offshore sand waves. *Coastal Engineering*, 53:265–275, 2006. doi: doi:10.1016/j.coastaleng.2005.10.014. URL `http://dx.doi.org/10.1016/j.coastaleng.2005.10.014`.

F.S.B.F. Oliveira. Assessment of open boundary conditions on the elliptic formulation of mild-slope equation. *Ocean Engineering*, 31:1567–1576, 2004.

V.G. Panchang and B.R. Pearce. Solution of the mild-slope equation by iteration. *Applied Ocean Research*, 13(4):187–198, 1991.

D. Peregrine. Interaction of water waves and currents. *Advances in Applied Mechanics*, 16:9–117, 1976.

A. Radder. On the parabolic equation method for water-wave propagation. *Journal of Fluid Mechanics*, 135:71–94, 1979.

Rijkswaterstaat. Waterbase. `http://live.waterbase.nl`, 2015. (Accessed in december 2015).

R. Santen, H. de Swart, and T. van Dijk. Sensitivity of tidal sand wavelength to environmental parameters: A combined data analysis and modellling approach. *Continental Shelf Research*, 31:966–978, 2011.

V. Santoro, E. Amore, L. Cavallaro, G. Cozzo, and E. Foti. Sand Waves in the Messina Strait. *Journal of Coastal Research*, SI36:640–653, 2002.

A. Sharifahmadian. *Numerical Models for Submerged Breakwaters: Coastal Hydrodynamics and Morphodynamics*, chapter 4, pages 61–64. Butterworth-Heinemann, 2015.

STW. SMARTSEA: Safe navigation by optimizing sea bed monitoring and waterway maintenance using fundamental knowledge of sea bed dynamics. `http://www.stw.nl/`, 2014.

J. Terwindt. Sand waves in the Southern bight of the North Sea. *Marine Geology*, 10: 51–67, 1971.

The Open University. Waves, Tides and Shallow-Water Processes. Butterworth-Heinemann, Oxford, 1999.

T. Tsay and P. Liu. A finite element model for wave refraction and diffraction. *Applied Ocean Research*, 5(1):30–37, 1983.

Appendix A

Mathematical background

A.1 Complex valued amplitude

The complex valued amplitude, which is also called a phasor, is the steady part of a complex wave signal and is solved in the Mild-Slope equation. The complex wave signal can be expressed in a Cartesian coordinate system (right hand term in Eq. (A.1)) or, by using Euler's Formula, in a polar coordinate system (left hand term in Eq. (A.1)). For a signal propagating to the right this results in the following expression:

$$Ae^{i(kx-\omega t+\varphi)} = \cos(kx - \omega t + \varphi) + i\sin(kx - \omega t + \varphi) \tag{A.1}$$

where A is the amplitude, $k = 2\pi/\lambda$ the wave number, $\omega = 2\pi/T$ the angular frequency and φ the phase. Taking the Real part of Eq. (A.1) will result in the surface elevation η. Further, the polar notation allows for separation of the arguments in the power. The latter means that the left hand side of Eq. (A.1) can be rewritten into a product of two complex wave signals as

$$Ae^{i(kx-\omega t+\varphi)} = Ae^{i(kx+\varphi)}e^{-i\omega t} \tag{A.2}$$

In case of monochromatic wave behaviour, there is no variation in the time-domain and hence $e^{-i\omega t}$ is not of interest. Therefore there can be chosen to only calculate the steady part, the phasor, of Eq. (A.2), $\hat{\eta}$, which is expressed as:

$$\hat{\eta} = Ae^{i(kx+\varphi)}. \tag{A.3}$$

The behaviour of the phasor is visualized in Figure A.1. In this figure it is visible that whenever the argument is a multiple of π, the Real part of the signal is at its crest or trough (i.e. maximum amplitude), and when on a multiple of $\pi/2$, the wave signal is at zero (i.e. no amplitude).

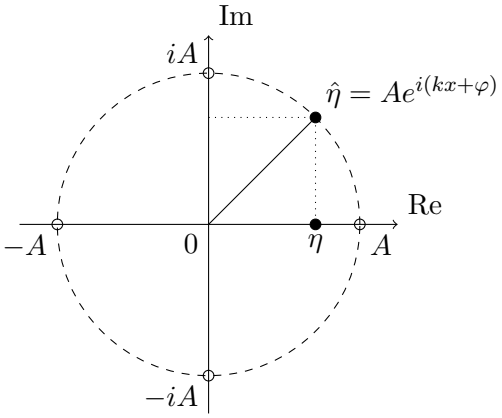

Figure A.1: Complex wave signal of the phasor $\hat{\eta} = Ae^{i(kx+\varphi)}$, for which the reflection on the Real (Re) axis represent the steady state surface elevation η which fluctuates between the amplitude A and $-A$.

A.2 Sparse matrix technique

The direct solution method as introduced in Section 2.4 first requires that the grid nodes are represented in a vector form rather than the current (n, m) index. Therefore re-indexing is required, which is done by the new index:

$$m^*(m, n) = m + (n - 1)M \tag{A.4}$$

Now, the system matrix of size $N^2 \times N^2$ can be filled with the coefficients from the discretized model equations. The row-number represents the grid node m^* which is being evaluated whereas the column-numbers are the m^* index of the neighbouring grid nodes. In case of a non-zero value in the matrix, a neighbour grid node influences the solution of the evaluated grid node. An example of an one dimensional, second order accurate system matrix of a Laplace problem is given in Eq. (A.5).

$$[V] = \begin{bmatrix} -2 & 1 & 0 & \cdots & 0 & 0 \\ 1 & -2 & 1 & \cdots & 0 & 0 \\ 0 & 1 & -2 & \ddots & 0 & 0 \\ \vdots & \vdots & \ddots & \ddots & 1 & 0 \\ 0 & 0 & 0 & 1 & -2 & 1 \\ 0 & 0 & 0 & 0 & 1 & -2 \end{bmatrix} \tag{A.5}$$

The example of the system matrix in Eq. (A.5) shows three non-zero diagonals, which means that each grid node is expressed by two neighbouring grids (coefficient of 1) and itself (coefficient of -2) whereas other grid nodes do not directly affect the evaluated grid node (coefficient of 0). Furthermore, the system matrix contains a significant number of zero-values.

Due to the relatively small wavelength of wind waves compared to the large extent of sand wave fields, the model must be able to solve a large numer of grid nodes in both x and y direction. When for example a $10^3 \times 10^3$ grid size is chosen, the system matrix contains $10^6 \times 10^6$ elements. When using the straight-forward way of mapping the system matrix (including all zero-values) as indicated in Eq. (A.5), the required RAM storage is in the order of tens of Terabytes, and therefore too big to solve on a personal computer[1].

To overcome this RAM requirement, the *sparse* matrix structure is used in our advantage. MATLAB has the ability to only store the non-zero values with its index in the system matrix and the size of the system matrix[2]. The example matrix in Eq. (A.5) then reduces to:

$$[V_{\text{sparse}}] = \begin{bmatrix} 1 & 1 & -2 \\ 2 & 1 & 1 \\ 1 & 2 & 1 \\ 2 & 2 & -2 \\ 3 & 2 & 1 \\ 2 & 3 & 1 \\ 3 & 3 & -2 \\ \vdots & \vdots & \vdots \\ N^2-1 & N^2 & 1 \\ N^2 & N^2 & -2 \end{bmatrix} \tag{A.6}$$

Due to storage of the system matrix in the sparse structure as given in Eq. (A.6), the RAM requirement reduces for the $10^3 \times 10^3$ grid size situation, to a manageable size of about 6 to 7 Gigabyte on a 64 bit computer.

Besides the system matrix $[V]$, also the known right-hand side vector $\{f\}$ needs to be stored. The discretized model equations in Eq. (2.18)-(2.23) have a right hand side of $f_{m^*} = 0$. However, the West boundary grid nodes, given by Eq. (2.20), have a right hand side equal to the scaled amplitude of the wind wave. Hence, in the right hand side vector $\{f\}$ the row-numbers corresponding to the m^* index of the Western grid nodes, are valued $\tilde{A}_0$. Furthermore, in the system matrix $[V]$, the Western grid nodes are independent of neighbours and therefore only have a central coefficient of 1.

Now that both the system matrix and the solution matrix can be filled, the unknown vector $\{\tilde{\eta}\}$ can be solved with Eq. (2.25). Subsequently, the two-dimensional representation of $\tilde{\eta}$ can be restored by the known combinations of (m, n) and m^*. Furthermore the complex valued amplitude $\hat{\eta}$ can be obtained by transforming back using Eq. (2.5).

[1] At the moment about 4 to 8GB RAM is the standard for a personal computer.

[2] In MATLAB this function is called `sparse()`.

A.3 Discretized model equations of second order accurate model

In this appendix the stencils used for the discretization of the second order accurate model are given. The interior grid nodes are approximated by a central space finite difference schematization:

$$1\tilde{\eta}_{x_{m-1},y_n} + 1\tilde{\eta}_{x_m,y_{n-1}} + (K^2_{x_m,y_n}\Delta^2 - 4)\tilde{\eta}_{x_m,y_n} + 1\tilde{\eta}_{x_{m+1},y_n} + 1\tilde{\eta}_{x_m,y_{n+1}} = 0. \tag{A.7}$$

The boundaries are expressed by one-sided finite differences:

$$\tilde{\eta}_{x_1,y_n} = \tilde{A}_0 \qquad \text{at}\Gamma_{\text{west}}, \tag{A.8}$$

$$\frac{3}{2}\tilde{\eta}_{x_m,y_N} - 2\tilde{\eta}_{x_m,y_{N+1}} + \frac{1}{2}\tilde{\eta}_{x_m,y_{N-2}} = 0 \qquad \text{at}\Gamma_{\text{north}}, \tag{A.9}$$

$$\left(\frac{3}{2} - iK_{x_N,y_n}\Delta\right)\tilde{\eta}_{x_N,y_n} - 2\tilde{\eta}_{x_N,y_{n+1}} + \frac{1}{2}\tilde{\eta}_{x_N,y_{n+2}} = 0 \qquad \text{at}\Gamma_{\text{east}}, \tag{A.10}$$

$$-\frac{3}{2}\tilde{\eta}_{x_m,y_1} + 2\tilde{\eta}_{x_m,y_2} - \frac{1}{2}\tilde{\eta}_{x_m,y_3} = 0 \qquad \text{at}\Gamma_{\text{south}}. \tag{A.11}$$

A.4 Wave numbers of an asymmetric sand wave profile

In this appendix, the derivation of the factors γ_{stoss} and γ_{lee} is given. First, from the relations in Figure 3.1 it can be seen that the following counts:

$$\lambda_b = \lambda_{b1} + \lambda_{b2}. \tag{A.12}$$

Furthermore the asymmetry factor S_b is repeated here:

$$S_b = \frac{\lambda_{b1}}{\lambda_{b2}}. \tag{A.13}$$

When combining Eq. (A.12) and (A.13) one can express the horizontal lengths of the stoss and lee side respectively as:

$$\lambda_{b1} = \frac{\lambda_b}{1 + S_b^{-1}}, \qquad \lambda_{b2} = \frac{\lambda_b}{1 + S_b}. \tag{A.14}$$

Now we should work towards an expression of:

$$k_{b1} = \gamma_{\text{stoss}} k_b, \qquad k_{b2} = \gamma_{\text{stoss}} k_b, \tag{A.15}$$

where k_{b1} and k_{b2} are the required wave numbers to create the sinusoids for the stoss and lee side respectively. We know that these wave numbers are equal to:

$$k_b = \frac{2\pi}{\lambda_b}, \qquad k_{b1} = \frac{2\pi}{2\lambda_{b1}}, \qquad k_{b2} = \frac{2\pi}{2\lambda_{b2}}. \tag{A.16}$$

Note that the required wavelength of the stoss and lee sinusoid corresponds to twice the horizontal length (λ_{b1}, λ_{b2}) of the stoss and lee side.

Now by substituting of Eq. (A.14) and (A.16) into (A.15), γ_{stoss} and γ_{lee} can be expressed as follows:

$$\gamma_{\text{stoss}} = \frac{1+S_b}{2S_b}, \qquad \gamma_{\text{lee}} = \frac{1+S_b}{2}. \tag{A.17}$$

A.5 Circular tapering function

First it is necessary to determine the center coordinates of the domain:

$$x_c = \frac{L}{2}, \qquad y_c = \frac{L}{2}, \tag{A.18}$$

where L is the length of the square domain. Subsequently, the tapering function can be described as:

$$w_{2D}(x,y) = \begin{cases} 0, & \text{if } r_{\text{var}} \geq (\frac{1}{2}-\gamma_0)L \\ \cos\left(\frac{\pi}{\gamma_t L}\left[(\frac{1}{2}-\gamma_0)L - r_{\text{var}}\right] - \pi\right), & \text{if } (\frac{1}{2}-\gamma_0-\gamma_t)L \leq r_{\text{var}} < (\frac{1}{2}-\gamma_0)L \\ 1, & \text{if } r_{\text{var}} < (\frac{1}{2}-\gamma_0-\gamma_t)L \end{cases}, \tag{A.19}$$

where $r_{\text{var}} = \sqrt{(x-x_c)^2+(y-y_c)^2}$ is the variable radius from the center coordinates, γ_0 is the ratio of the domain used for the flat-bed configuration and γ_t is the ratio of the domain used for the transition zone (see Figure 3.4 for reference).

Appendix B

Visualization of Spatial Variability: sinh(kh)

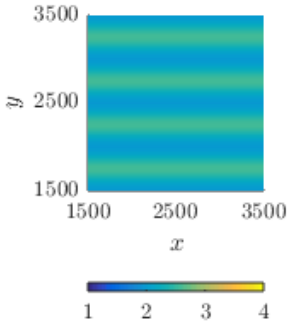

Figure B.1: Visualization of spatial variability of sinh(kh) corresponding to Figure 4.2: base case.

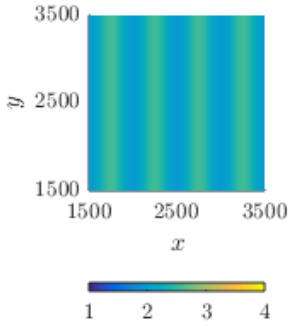

Figure B.2: Visualization of spatial variability of sinh(kh) corresponding to Figure 4.3: base case with $\theta_b = 0$ degrees.

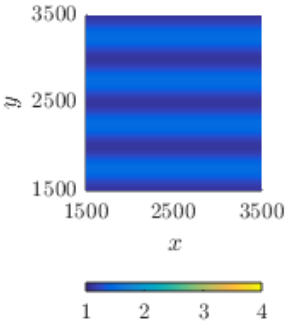

Figure B.3: Visualization of spatial variability of sinh(kh) corresponding to Figure 4.4: base case with $\bar{h} = 12$ meter.

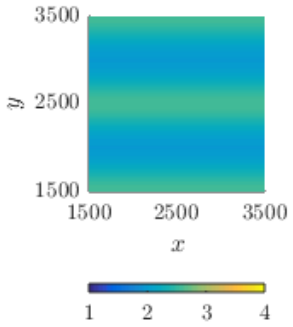

Figure B.4: Visualization of spatial variability of $\sinh(kh)$ corresponding to Figure 4.5: base case with $\lambda_b = 1000$ meter.

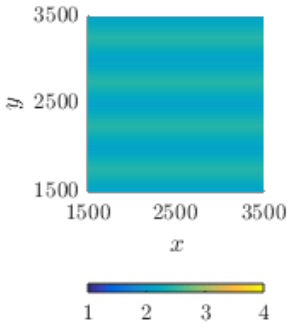

Figure B.5: Visualization of spatial variability of $\sinh(kh)$ corresponding to Figure 4.6: base case with $H_b = 2$ meter.

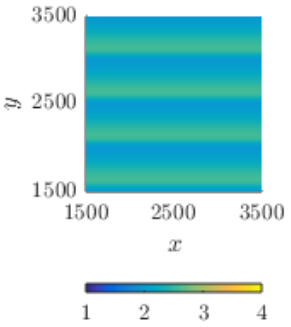

Figure B.6: Visualization of spatial variability of $\sinh(kh)$ corresponding to Figure 4.7: base case with $S_b = 3$.

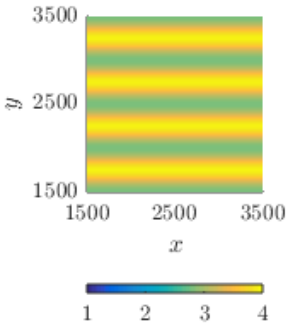

Figure B.7: Visualization of spatial variability of $\sinh(kh)$ corresponding to Figure 4.8: base case with $T = 7$ seconds.

Appendix C

Graphs showing the distribution of spatial variability

In this appendix, the distribution of the Amplification Factors of wind wave amplitude and near-bed orbital flow velocity above the sand wave crests, troughs and above the whole area of interest are given. Each figure is characterized by the base case configuration where the parameter on the x axis is being changed and assessed.

(a) Amplification of wind wave amplitude above sand wave crests

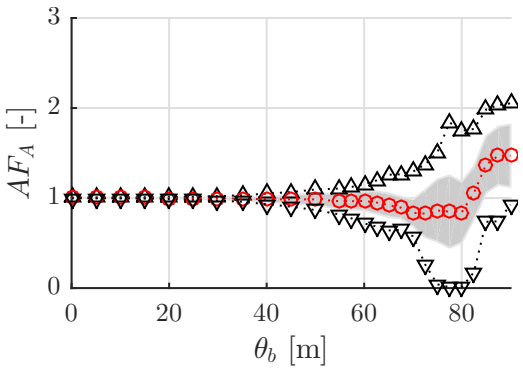

(b) Amplification of near-bed flow velocity above sand wave crests

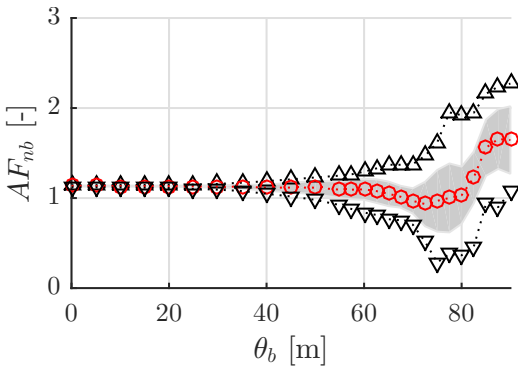

(c) Amplification of wind wave amplitude above sand wave troughs

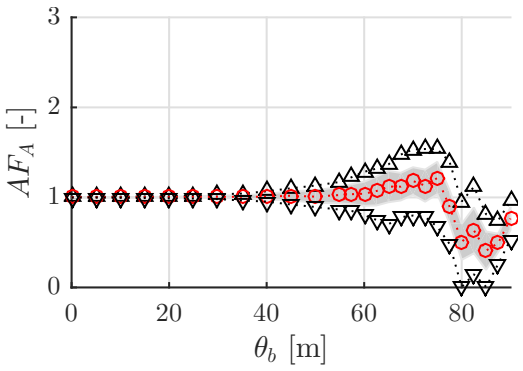

(d) Amplification of near-bed flow velocity above sand wave troughs

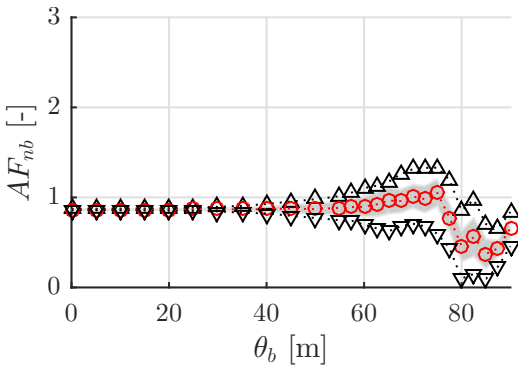

(e) Amplification of wind wave amplitude above area of interest

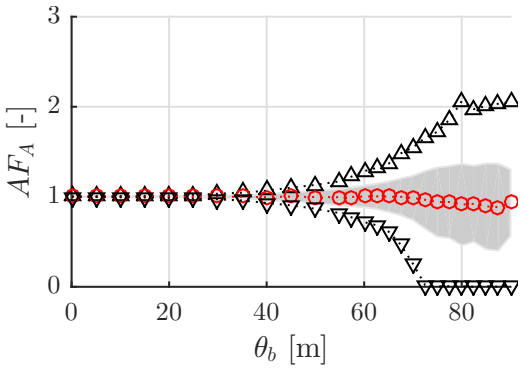

(f) Amplification of near-bed flow velocity above area of interest

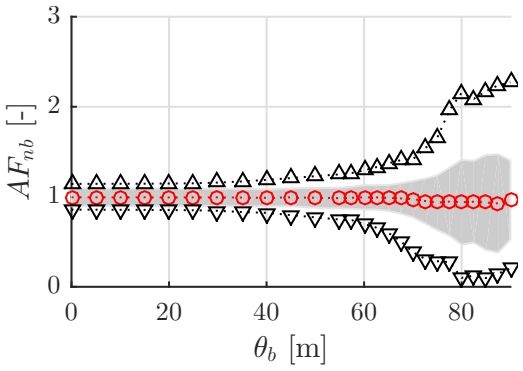

Figure C.1: Spatial distribution of the base case with a variable orientation. The symbols denote: △ max, ▽ min, ◯ mean and the gray area shows the standard deviation.

(a) Amplification of wind wave amplitude above sand wave crests

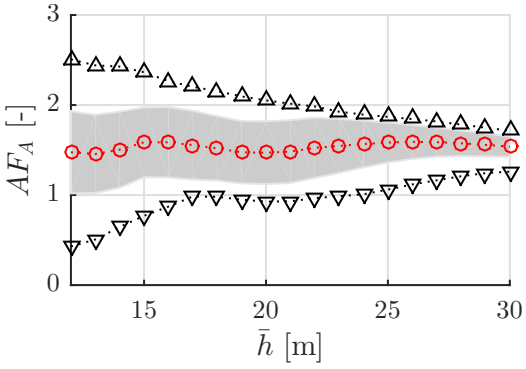

(b) Amplification of near-bed flow velocity above sand wave crests

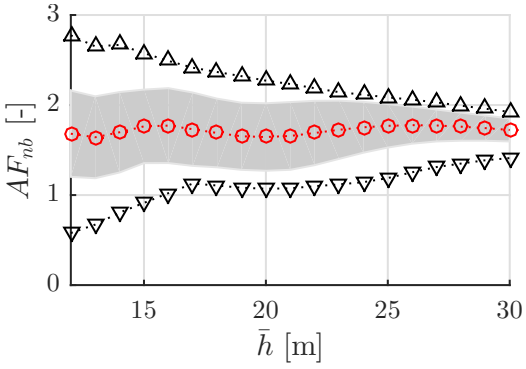

(c) Amplification of wind wave amplitude above sand wave troughs

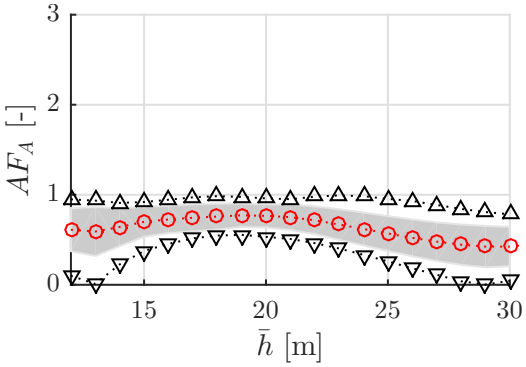

(d) Amplification of near-bed flow velocity above sand wave troughs

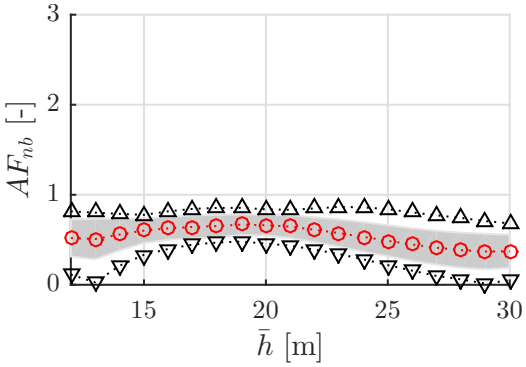

(e) Amplification of wind wave amplitude above area of interest

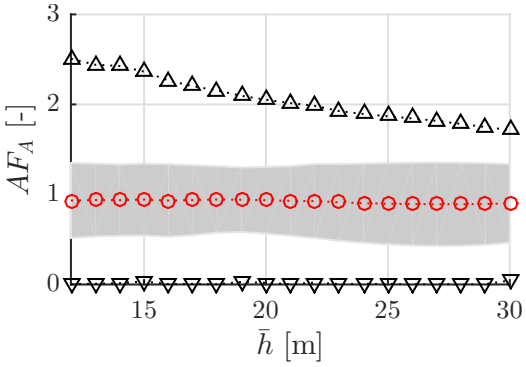

(f) Amplification of near-bed flow velocity above area of interest

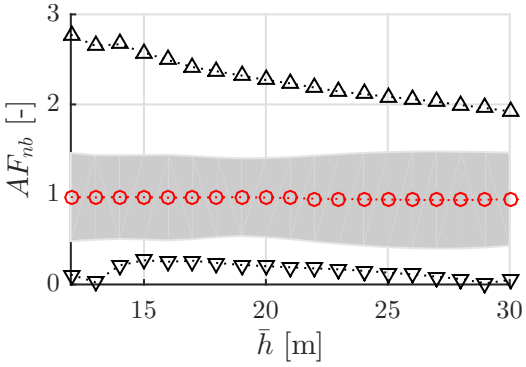

Figure C.2: Spatial distribution of the base case with a variable water depth. The symbols denote: △ max, ▽ min, ◯ mean and the gray area shows the standard deviation.

(a) Amplification of wind wave amplitude above sand wave crests

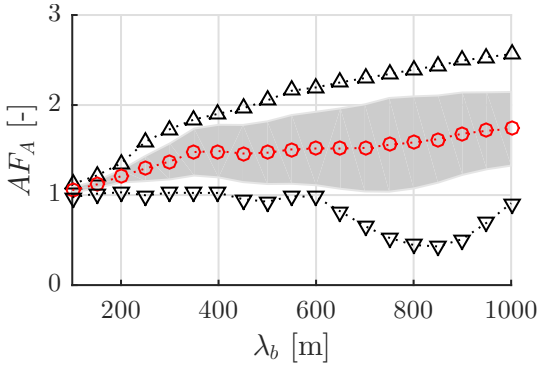

(b) Amplification of near-bed flow velocity above sand wave crests

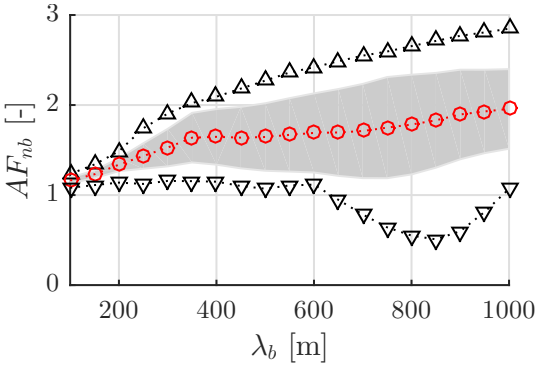

(c) Amplification of wind wave amplitude above sand wave troughs

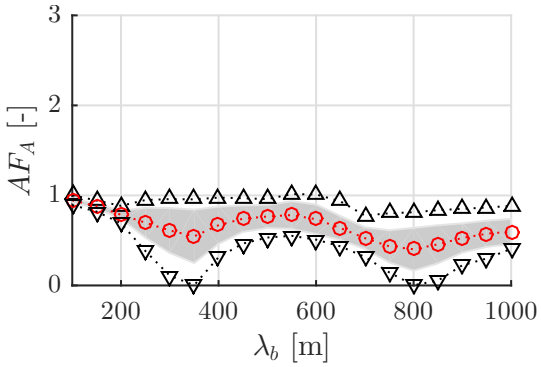

(d) Amplification of near-bed flow velocity above sand wave troughs

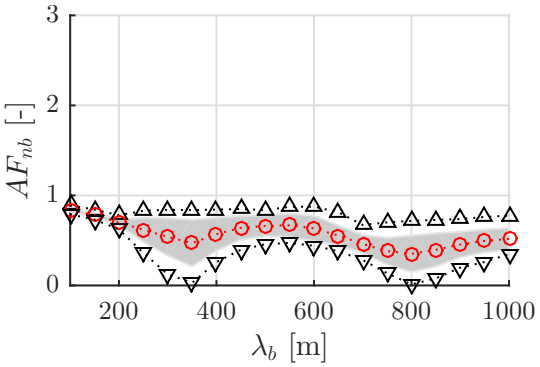

(e) Amplification of wind wave amplitude above area of interest

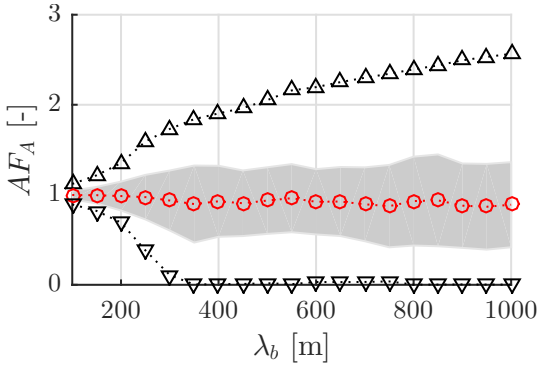

(f) Amplification of near-bed flow velocity above area of interest

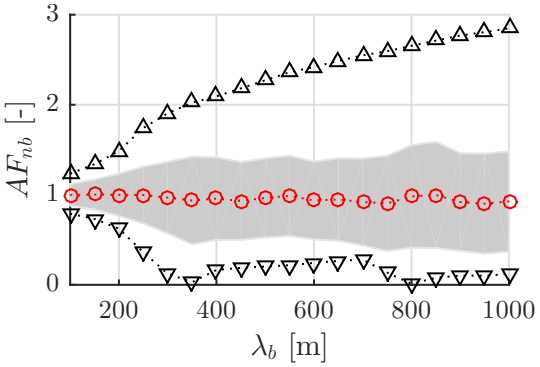

Figure C.3: Spatial distribution of the base case with a variable sand wave length. The symbols denote: △ max, ▽ min, ◯ mean and the gray area shows the standard deviation.

(a) Amplification of wind wave amplitude above sand wave crests

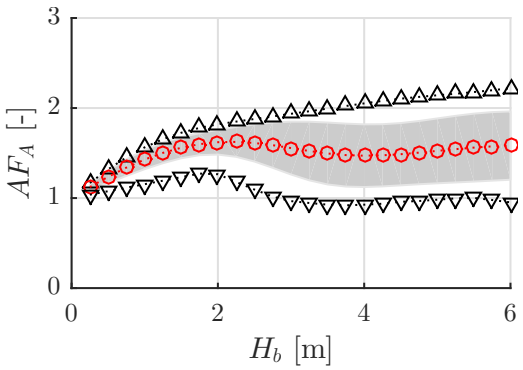

(b) Amplification of near-bed flow velocity above sand wave crests

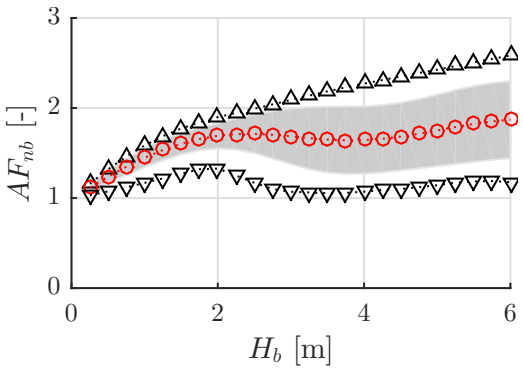

(c) Amplification of wind wave amplitude above sand wave troughs

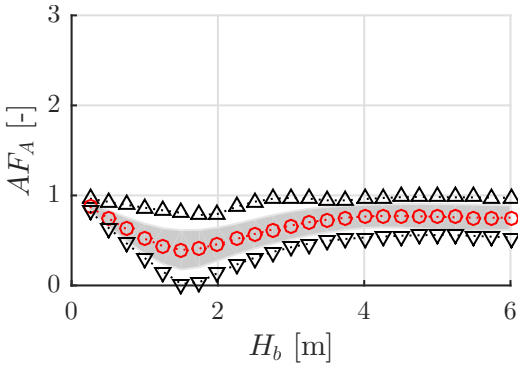

(d) Amplification of near-bed flow velocity above sand wave troughs

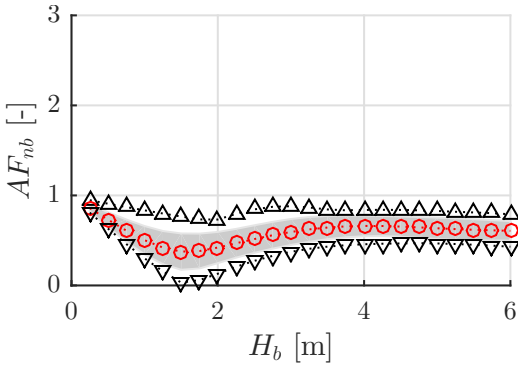

(e) Amplification of wind wave amplitude above area of interest

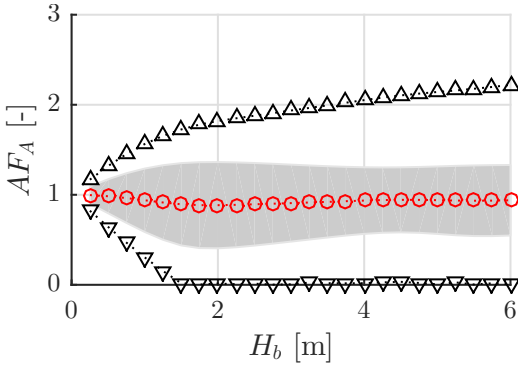

(f) Amplification of near-bed flow velocity above area of interest

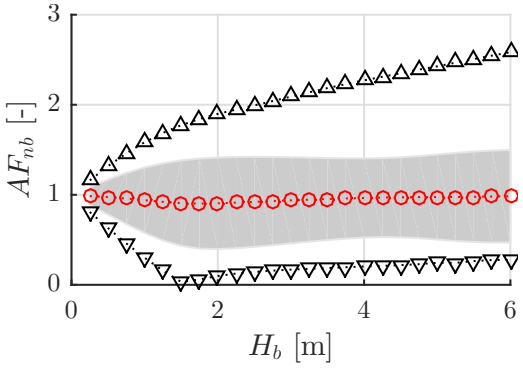

Figure C.4: Spatial distribution of the base case with a variable sand wave height. The symbols denote: △ max, ▽ min, ◯ mean and the gray area shows the standard deviation.

(a) Amplification of wind wave amplitude above sand wave crests

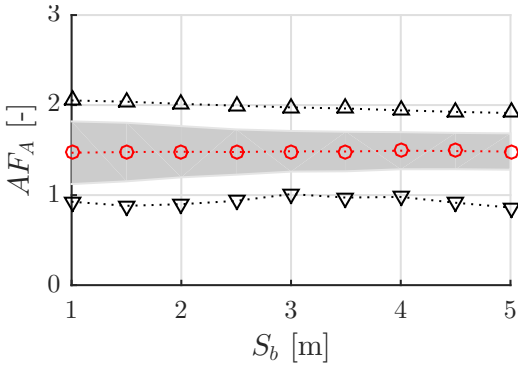

(b) Amplification of near-bed flow velocity above sand wave crests

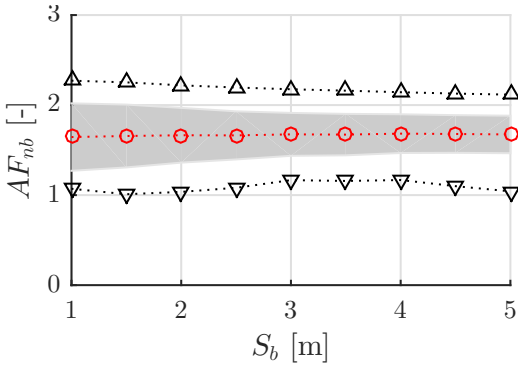

(c) Amplification of wind wave amplitude above sand wave troughs

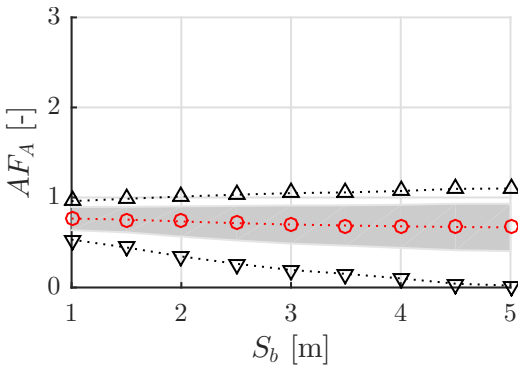

(d) Amplification of near-bed flow velocity above sand wave troughs

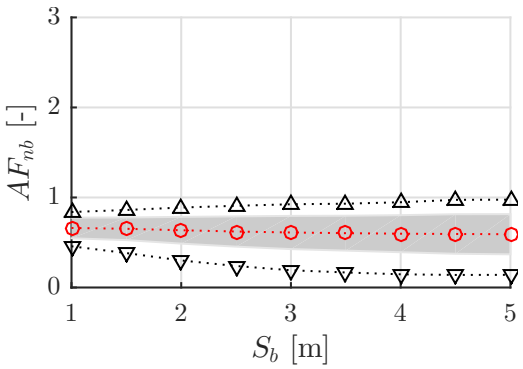

(e) Amplification of wind wave amplitude above area of interest

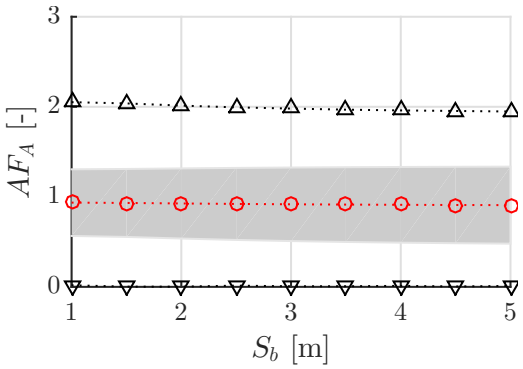

(f) Amplification of near-bed flow velocity above area of interest

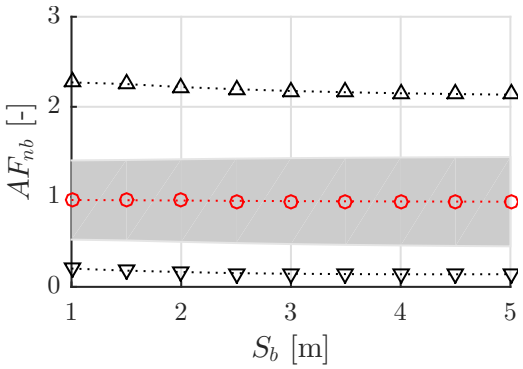

Figure C.5: Spatial distribution of the base case with a variable asymmetry factor of the sand waves. The symbols denote: △ max, ▽ min, ◯ mean and the gray area shows the standard deviation.

(a) Amplification of wind wave amplitude above sand wave crests

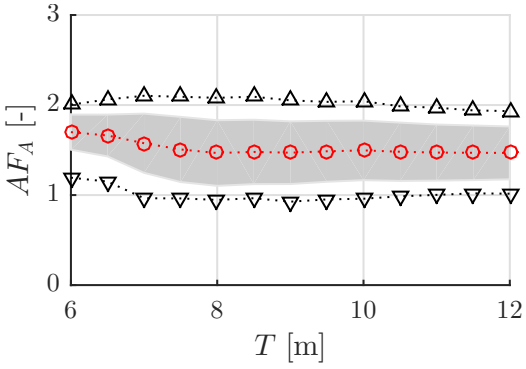

(b) Amplification of near-bed flow velocity above sand wave crests

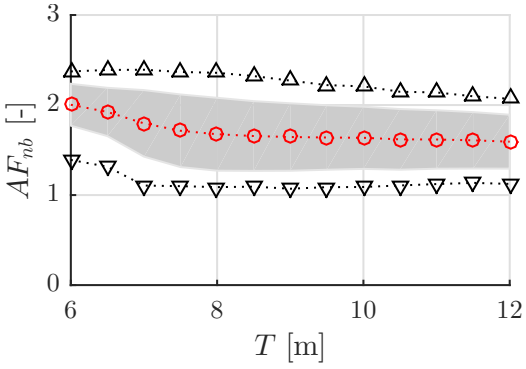

(c) Amplification of wind wave amplitude above sand wave troughs

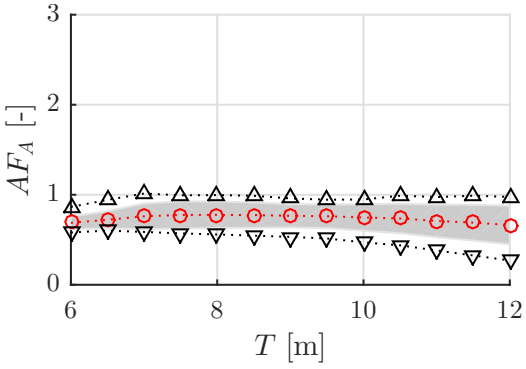

(d) Amplification of near-bed flow velocity above sand wave troughs

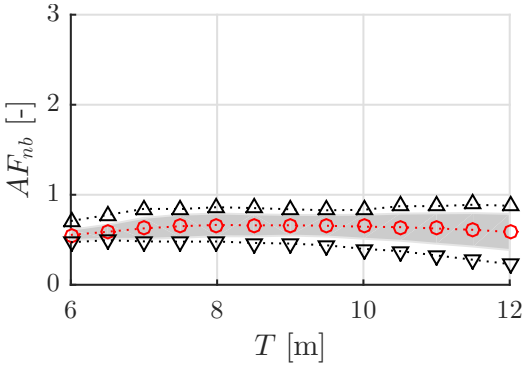

(e) Amplification of wind wave amplitude above area of interest

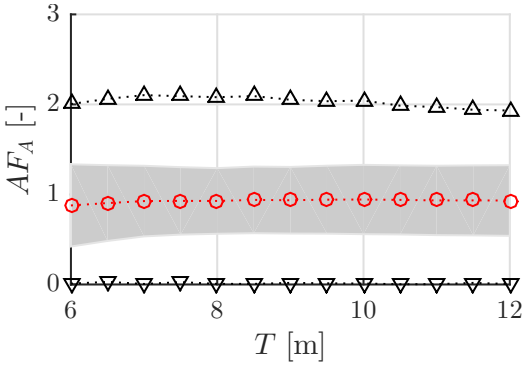

(f) Amplification of near-bed flow velocity above area of interest

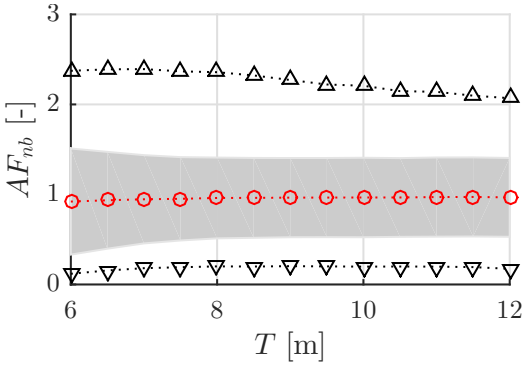

Figure C.6: Spatial distribution of the base case with a variable wind wave period. The symbols denote: △ max, ▽ min, ◯ mean and the gray area shows the standard deviation.

Appendix D

Dimensionless form of the Mild-Slope Equation

First the Mild-Slope Equation in its dimension full, according to Berkhoff (1976), is repeated here:

$$\nabla \cdot (cc_g \nabla \hat{\eta}) + k^2 cc_g \hat{\eta} = 0. \tag{D.1}$$

Now we choose to scale the wave number k with the mean water depth $\bar{h}$ such that the following counts:

$$k = \frac{k^*}{\bar{h}}, \tag{D.2}$$

where k^* is the dimensionless wave number for the flat-bed configuration. Also we scale the variable water depth with the mean water depth:

$$h = h^* \bar{h} \tag{D.3}$$

where h^* is the dimensionless variable water depth. Furthermore, we scale the complex valued amplitude $\hat{\eta}$ by the predefined amplitude of the incident wind wave A_0 as follows:

$$\hat{\eta} = \hat{\eta}^* A_0, \tag{D.4}$$

where $\hat{\eta}^*$ is a dimensionless complex valued amplitude (i.e. note that throughout this thesis $|\hat{\eta}|/A_0 = \mathrm{AF}$). Lastly, we scale the Cartesian coordinate system by a sand wave length λ_b, hence:

$$x = x^* \lambda_b, \qquad y = y^* \lambda_b, \qquad \nabla = \frac{\nabla^*}{\lambda_b}, \tag{D.5}$$

where x^*, y^* and ∇^* represent the dimensionless coordinate system.

Subsequently, with the dispersion relationship from Linear Wave Theory and use of Eq. (D.2) the phase and group celerity can be expressed as follows:

$$c = c^* \sqrt{gh}, \qquad c^* = \sqrt{\frac{\tanh(k^* h^*)}{k^* h^*}} \tag{D.6}$$

$$c_g = c_g^* \sqrt{gh}, \qquad c_g^* = \frac{c^*}{2}\left[1 + k^* h^* \frac{1 - \tanh^2(k^* h^*)}{\tanh(k^* h^*)}\right] \tag{D.7}$$

Now, when substituting Eq. (D.2) to (D.7) into Eq. (D.1), the following dimensionless form of the Mild-Slope Equation results:

$$\nabla^* \cdot \left(c^* c_g^* \nabla^* \hat{\eta}^*\right) + \Theta^2 {k^*}^2 c^* c_g^* \hat{\eta}^* = 0, \tag{D.8}$$

where $\Theta = \lambda_b / \bar{h}$.

Now, when different sets of parameters, consisting of θ_b, λ_b, H_b, S_b, $\bar{h}$, A_0 and T, produce the same values for k^*, Θ, S_b and θ_b, the Mild-Slope Equation mathematically shows the same behaviour.

However, due to the sand wave field patch, the size of this patch also influences the mild-slope equation and therefore still differences might be present as this size is not included in the scaling procedure.